Embedding Fe-Nx Structure in Porous Carbon Nanospheres for Enhanced CO2 Electroreduction to CO

Author:
Shi, Zhen

Publication Date:
2021

DOI:
https://doi.org/10.26190/unsworks/1968

Embedding Fe-N_x Structure in Porous Carbon Nanospheres for Enhanced CO_2 Electroreduction to CO

This thesis in fulfilment of the requirements for the degree of

Master by Research

By

Zhen Shi

UNSW
AUSTRALIA

School of Chemistry

Faculty of Science

September 2021

THE UNIVERSITY OF NEW SOUTH WALES

Thesis/Dissertation Sheet

Surname or Family name: Shi

First name: Zhen

Other name/s: N/A

Abbreviation for degree as given in the University calendar: MRes

School: School of Chemistry **Faculty: Science**

Title: Embedding Fe-N_x Structure in Porous Carbon Nanospheres for Enhanced CO_2 Electroreduction to CO

Abstract 350 words maximum:

Electrochemical reduction of carbon dioxide (CO_2ER) reaction has become an attractive and promising approach to convert CO_2 into fuels and high-value-added chemicals. However, the electrochemical reduction of CO_2 suffers from sluggish reaction kinetics and poor product selectivity. Therefore, the development of efficient catalysts with high electrochemical catalytic ability and selectivity is in high demand. To this regard, this thesis aims to develop a novel embedded Fe-N_x structure in porous carbon nanospheres as catalysts for efficient CO_2ER, and to disclose the relationship between enhanced for efficiency and structural regulation.

In Chapter 1, current catalysts for electrochemical reduction CO_2 have been systematically reviewed including metallic-based materials, metal oxides, transition-metal dichalcogenides, single-atom confined materials, and metal-free carbon-based materials. The conversions from CO_2 into diversities of products were also discussed according to the relevant catalytic process.

Chapter 2 gives the experimental details for this research project, including the chemicals, devices, fabrications of the catalysts and the testing protocols for physical characterizations and electrochemical performance of the as-prepared materials.

Chapter 3 develops a novel catalyst for CO_2 conversion into CO. 5,10,15,20-Tetraphenyl-21H,23H-porphine iron (III) chloride (Fe-TPP precursor) was embedded into zeolitic imidazolate framework-8 (ZIF-8) and finally obtained a Fe-N_x structure onto porous carbon nanosphere. The porous carbon nanospheres were prepared by a silica-protected strategy. The content of active sites Fe-N_x exposed for efficient catalysis is quite limited, which hinder the performance of catalysts. The hierarchical porous structures expose more Fe-Nx sites, which would enhance the properties of Fe-N_x-C catalysts. The local pH change near the catalyst surface and the influence of mesoporosity are also investigated. The results indicate that the mesoporosity can boost CO_2 and proton diffusion and improve CO current density for CO_2ER.

Chapter 4 summarises the research findings and also offers several perspectives for enhancing CO_2ER in the future.

Declaration relating to disposition of project thesis/dissertation

I hereby grant to the University of New South Wales or its agents the right to archive and to make available my thesis or dissertation in whole or in part in the University libraries in all forms of media, now or here after known, subject to the provisions of the Copyright Act 1968. I retain all property rights, such as patent rights. I also retain the right to use in future works (such as articles or books) all or part of this thesis or dissertation.

I also authorise University Microfilms to use the 350-word abstract of my thesis in Dissertation Abstracts International (this is applicable to doctoral theses only).

Signature Witness Signature Date

The University recognises that there may be exceptional circumstances requiring restrictions on copying or conditions on use. Requests for restriction for a period of up to 2 years must be made in writing. Requests for a longer period of restriction may be considered in exceptional circumstances and require the approval of the Dean of Graduate Research.

Date of completion of requirements for Award:

FOR OFFICE USE ONLY

COPYRIGHT STATEMENT

Signed.....

Date.....

AUTHENTICITY STATEMENT

Signed.....

Date.....

ORIGINALITY STATEMENT

‘I hereby declare that this submission is my own work and to the best of my knowledge it contains no materials previously published or written by another person, or substantial proportions of material which have been accepted for the award of any other degree or diploma at UNSW or any other educational institution, except where due acknowledgement is made in the thesis. Any contribution made to the research by others, with whom I have worked at UNSW or elsewhere, is explicitly acknowledged in the thesis. I also declare that the intellectual content of this thesis is the product of my own work, except to the extent that assistance from others in the project's design and conception or in style, presentation and linguistic expression is acknowledged.’

Signed.....

Date.....

INCLUSION OF PUBLICATIONS STATEMENT

UNSW is supportive of candidates publishing their research results during their candidature as detailed in the UNSW Thesis Examination Procedure.

Publications can be used in their thesis in lieu of a Chapter if:

- The candidate contributed greater than 50% of the content in the publication and is the "primary author", ie. the candidate was responsible primarily for the planning, execution and preparation of the work for publication.
- The candidate has approval to include the publication in their thesis in lieu of a Chapter from their supervisor and Postgraduate Coordinator.
- The publication is not subject to any obligations or contractual agreements with a third party that would constrain its inclusion in the thesis.

Please indicate whether this thesis contains published material or not:

☒ This thesis contains no publications, either published or submitted for publication.

☐ Some of the work described in this thesis has been published and it has been documented in the relevant Chapters with acknowledgement.

☐ This thesis has publications (either published or submitted for publication) incorporated into it in lieu of a chapter and the details are presented below.

CANDIDATE'S DECLARATION

I declare that:

- I have complied with the UNSW Thesis Examination Procedure
- where I have used a publication in lieu of a Chapter, the listed publication(s) below meet(s) the requirements to be included in the thesis.

Candidate's Name	**Signature**	**Date (dd/mm/yy)**
Zhen Shi		

ACKNOWLEDGEMENTS

First of all, I would like to express my sincere gratitude to my supervisor, Prof. Chuan Zhao, for his strong support on my research project. It is my great pleasure to study in his group for investigation on electrochemical carbon dioxide reduction. His meticulous and enthusiastic attitude toward academic research has helped me to fundamentally understand the intricacies of research work. Prof. Zhao has demonstrated his incredible care and commitment to me and guided this project with his proficient supervision. Most importantly, I would like to thank him for his patience and support in response to the coronavirus (COVID 19) during this challenging time.

I would like to express my gratitude to Dr Yong Zhao, for his generous contribution to the scope of this project with his knowledge and experience in CO_2 electroreduction. I have gained valuable details on experiments and theories, which are essential and fundamental to the completion of this project.

I would also like to thank all the members of Chuan's group. Dr Sam Chen, Dr Quentin Meyer, Dr Yuan Wang and Muhannad Ibrar Ahmed. My tremendous gratitude to the group for lab management and tireless assistance. Another special thanks to Dr Xin Bo, Dr William Adamson, Dr Mengchen Ge, Dr Wangfeng Yang, Dr Chen Jia, Dr Karin Ching, Tim Fang, Zhen Su, Qian Sun, Tingwen Zhao,Xinyi Zhang, Shiyang Liu, Chiengli Rong, Sicheng Wu, Xuancheng Peng, Haocheng Guo and Yang Xiao. These friendships have become important 'treasures' in both my academic and personal life.

I am also very grateful for the support of my old friends, Liangju Chen, Zhenwei Peng, Xinjue Chen, Yingyan Tang. Their encouragement and comfort have helped me overcome obstacles and challenges during difficult times.

Most importantly, I would like to express my utmost gratitude to my parents. Their endless love and support to my life and study have been very important and meaningful to the completion of my degree.

Finally, I want to thank and recognise the support I have received so that I have the opportunity to complete this thesis successfully during the pandemic. I also believe the panic must turnover, and a much brighter future is always in front of us. May the peace and love be with you all.

Zhen Shi

14/08/2021

ABSTRACT

Electrochemical reduction of carbon dioxide (CO_2ER) reaction has become an attractive and promising approach to convert CO_2 into fuels and high-value-added chemicals. However, the electrochemical reduction of CO_2 suffers from sluggish reaction kinetics and poor product selectivity. Therefore, the development of efficient catalysts with high electrochemical catalytic ability and selectivity is in high demand. To this regard, this thesis aims to develop a novel embedded Fe-N_x structure in porous carbon nanospheres as catalysts for efficient CO_2ER, and to disclose the relationship between enhanced for efficiency and structural regulation.

In Chapter 1, current catalysts for electrochemical reduction CO_2 have been systematically reviewed including metallic-based materials, metal oxides, transition-metal dichalcogenides, single-atom confined materials, and metal-free carbon-based materials. The conversions from CO_2 into diversities of products were also discussed according to the relevant catalytic process.

Chapter 2 gives the experimental details for this research project, including the chemicals, devices, fabrications of the catalysts and the testing protocols for physical characterizations and electrochemical performance of the as-prepared materials.

Chapter 3 develops a novel catalyst for CO_2 conversion into CO. 5,10,15,20-Tetraphenyl-21H,23H-porphine iron (III) chloride (Fe-TPP precursor) was embedded into zeolitic imidazolate framework-8 (ZIF-8) and finally obtained a Fe-N_x structure onto porous carbon nanosphere. The porous carbon nanospheres were prepared by a

silica-protected strategy. The content of active sites Fe-N_x exposed for efficient catalysis is quite limited, which hinder the performance of catalysts. The hierarchical porous structures expose more Fe-Nx sites, which would enhance the properties of Fe-N_x-C catalysts. The local pH change near the catalyst surface and the influence of mesoporosity are also investigated. The results indicate that the mesoporosity can boost CO_2 and proton diffusion and improve CO current density for CO_2ER.

Chapter 4 summarises the research findings and also offers several perspectives for enhancing CO_2ER in the future.

LIST OF ABBREVIATIONS

CO_2ER	CO_2 Electrochemical Reduction
CRR	CO_2 Reduce Reaction
HER	Hydrogen Evolution Reaction
RHE	Reversible Hydrogen Electrode
C_{dl}	Double Layer Capacitance
ECSA	Electrochemical Surface Area
FE	Faradaic Efficiency
DFT	Density Functional Theory
EIS	Electrochemical Impedance Spectroscopy
FID	Flame Ionization Detector
GC	Gas Chromatography
TCD	Thermal conductivity Detector
NPs	Nanoparticles
GO	Graphene Oxide
RRDE	Rotating Ring-Disk Electrode
EDS	Energy-Dispersive X-ray Spectroscopy
BET	Brunauer-Emmett-Teller
LSV	Linear Sweep Voltammetry
HAADF	High-Angle Annular Dark-Field
NMR	Nuclear Magnetic Resonance

SHE	Standard Hydrogen Electrode
XRD	Xay-ray Diffraction
XPS	X-ray Photoelectron Spectroscopy
TEM	Transmission Electron Microscope
STEM	Scanning Transmission Electron Microscope
NWs	Nanowires
A	Ampere
cm	Centimeter
F	Faraday
CCU	Carbon Dioxide Capture and Utilization
h	hour
M	Mole per litre
mA	Milliampere
mV	Millivolt
min	Minute
nm	Nanometer
s	Second
V	Volt
Ω	Ohm
μ	Micro
L	Litre
ml	Millilitre

LIST OF FIGURES

Figure	Caption
1.1	Scheme of a CO_2ER Homogeneous Electrocatalyst. Reproduced with permission. Copyright 2018, John Wiley and Sons.
1.2	Schematic illustrates the electrolyzer for CO_2ER
1.3	Possible reaction mechanism of electrochemical CO2 reduction on various metal electrodes in aqueous solutions. Redrawn according to reference. Copyright 2018, John Wiley and Sons.
1.4	Schematic illustration for the proposed pathway of the CO_2 reduction to CO on the TiO_2 supported Ag NPs. Reproduced with permission. Copyright 2014, John Wiley and Sons.
1.5	(a)HAADF image and LAADF image (inset) for MoS_2 edges (scale bar, 5 nm) (b) The line scans for MoS_2 to prove the Mo atom as ending ; (c) LSV curves of bulk Ag (green line), Ag NPs (blue line), and bulk MoS_2 (green line) (d) FE_{CO} and FE_{H2} for bulk MoS_2; (e) Annual bright-field STEM (VA MoS_2 scale bar,20nm), and inset image is STEM for VA MoS_2 (scale bar 50nm); (f) bulk MoS_2 and VA MoS_2 nanosheets CO_2ER performance. Adapted with permission. Copyright 2014, Nature Publishing Group.
1.6	(a), (b) SEM images for N-CNFs; (c) CVs curves for carbon electrode and CNTs electrode in pure EMIM-BF_4 electrolyte with Ar and CO_2 saturated. (d) The current density for CO_2ER at different electrodes in CO_2 saturated

pure EMIM-BF_4 electrolyte. (e) Schematic illustration of the CO_2ER mechanism for N-CNFs. Reproduced with permission Copyright 2013, Nature Publishing Group

1.7 a-c) Faradic Efficient (FE) for H_2, CO, and CH_4 at the different applied potential with IR-corrected. d) Catalyst mass-normalized CO partial current for five types of M-N-C catalysts, which were compared with the Au catalysts (properties ranges for Au-nanoparticles and Au-nanowires are represented by filled regions). Reproduced with permission. Copyright 2017, Publishing Group

1.8 A) fabrication of m-SnO_2 catalyst B) TEM images for m-SnO_2 C) high-magnification for m-SnO_2 D) FE of $HCOO^-$ for m-SnO_2, SnO_2 NPs and SnO_2/C NPs E) partial current density for $HCOO^-$ for m-SnO_2 SnO_2 NPs and SnO_2/C. Copyright 2018 Elsevier.

2.1 Applied linearly changing voltage and corresponding varying current.

2.2 The image of on-line analysis system for CO_2ER.

2.3 Peak areas and the corresponding concentration curves for GC, a) H_2, b) CO, c) CH_4, d) C_2H_4, e) C_2H_6.

2.4 Photo of the standard three-electrode system in PEM H-Cell

3.1 Figure 3.1 a) SEM image for the Nano-SiO_2@ZIF-8 core-shell. b) SEM image for the nano-ZnO sphere. c) SEM image for nano-ZnO@ZIF-8 core-shell. d) SEM image for N-doped carbon with the template removal.

3.2 a) Scheme illustration for synthesis pathway for p-Fe-N_x-C and s-Fe-N_x-

C. b) HAAF-STEM image of p-Fe-N_x-C, c) SEM image of p-Fe-N_x-C. d) HAADF-STEM image of s-Fe-N_x-C, e) SEM image for s-Fe-N_x-C. f) High-resolution HAAF-STEM image for p-Fe-N_x-C. g) EDS mapping for p-Fe-N_x-C. h) pore size distribution for p-Fe-N_x-C and s-Fe-N_x-C.

3.3 a) aberration-corrected HAADF-STEM image for s-Fe-N_x-C. b) EDS spectrum for s-Fe-N_x-C.

3.4 a) High-resolution XPS N 1s spectrum, b) High-resolution Fe 2p, c) XRD patterns, d) Raman spectra, for s-Fe-N_x-C and p-Fe-N_x-C.

3.5 a) LSV curves of the carbon paper, s-Fe-N_x-C and p-Fe-N_x-C. b) Faradaic efficiency for CO, c) j_{co} of s-Fe-N_x-C and p-Fe-N_x-C. d) ECSA of s-Fe-N_x-C and p-Fe-N_x-C e) ECSA-normalized j_{co} of s-Fe-N_x-C and p-Fe-N_x-C. f) TOFs of s-Fe-N_x-C and p-Fe-N_x-C

3.6 a) Nquist plots tested in CO_2-saturated 0.5M $KHCO_3$ aqueous solutions at 0V vs. RHE, b) CO Faradaic efficiencies on the different P_{CO2} at -0.5V vs. RHE, c) P_{CO2} dependence of the CO partial current densities at-0.5V vs RHE for p-Fe-N_x-C, s-Fe-N_x-C, d) Scheme illustration for RRDE, e) Cyclic voltammograms (CVs) of CO oxidation collected by the Pt ring electrode, f) Observed peak potential E_{peak}.

LIST OF TABLES

Table	Caption
1.1	Standard potentials of CO_2 reduction reaction in aqueous solutions (V vs. SHE) at pH=7, 1.0 atm and 25^oC
1.2	Performance for alloy catalysts toward CO_2ER. Modified according to reference
1.3	Summary of the properties for metal-free carbon catalysts toward CO_2ER from recently reports.
1.4	Summary of the properties of single-atoms catalysts for CO_2ER toward CO
2.1	Materials Details
3.1	BET results of catalysts.
3.2	ICP-OES-results for the p-Fe-N_x-C and s-Fe-N_x-C

CONTENTS

ACKNOWLEDGEMENTS I

ABSTRACT III

LIST OF ABBREVIATIONS V

LIST OF FIGURES VII

LIST OF TABLES X

CONTENTS XI

Chapter 1 Introduction 1

1.1 Background 1

1.2 Introduction of CO_2ER 2

1.2.1 Homogenous Catalysts 2

1.2.2 Heterogeneous Catalysts 3

1.2.2.1 Thermodynamics and Kinetics of Heterogeneous CO_2ER 4

1.2.2.2 Significant Index to Evaluate Heterogeneous CO_2ER 6

1.2.2.3 Challenges of Heterogeneous Catalysts 8

1.3 Current Heterogeneous Catalysts for CO_2ER 9

1.3.1 Metal Catalyst 10

1.3.1.1 Bulk Metals Catalyst 10

1.3.1.2 Nanostructured Metals 12

1.3.1.3 Metal Alloys Catalysts 13

1.3.2 Metal Oxides 15

1.3.3 Transition-Metal Dichalcogenide Catalysts 16
1.3.4 Metal-Free Carbon Catalysts 18
1.3.5 Single-Atom Catalysts 21
1.4 Importance of Porous Structure 27
1.5 Synthesis Method for Porosity in carbon-based Materials 31
1.6 Thesis Objective 31
Chapter 2 Experimental Methods 33
2.1 Materials 33
2.2 Materials Characterizations Technique 34
2.2.1 Physical Characterizations 34
2.2.1.1 Scanning Electron Microscopy 35
2.2.1.2 TEM, STEM, HAADF-STEM, EDS 35
2.2.1.3 X-ray Photoelectron Spectroscopy 36
2.2.2 Electrochemical Characterization 37
2.2.2.1 LSV 37
2.2.2.2 CPA 37
2.2.2.3 Experiment Measurements 38
2.3 Identification of CO_2 Product 38
2.3.1 Gaseous Products Analysis 39
Chapter 3 Atomically dispersed Fe-N_x sites on Mesoporous Carbon with Enhance Mass Transport for Selective CO_2 Electroreduction. 43
3.1 Introduction 43

3.2 Experiment Section 44
3.2.1 Materials 44
3.2.2 Catalyst preparation 45
3.2.2.1 Synthesis of Nano-SiO_2@ZIF-8 Core-shell Material 45
3.2.2.2 Synthesis of Nano-ZnO@ZIF-8 Core-shell Materials 45
3.2.2.3 Synthesis of Zeolitic Imidazolate Framework-8 (ZIF-8) 46
3.2.2.4 Synthesis of SiO_2 Coated ZIF-8 Nanoparticles (SiO_2@ZIF-8) ... 46
3.2.2.5 Synthesis of Fe-N_x-C with Porosity (p-Fe-N_x-C) 47
3.2.2.6 Synthesis of Fe-N_x-C without Porosity (s-Fe-N_x-C) 47
3.3 Results and Discussion 48
3.4 Conclusion 61
Chapter 4 Conclusion and Outlook 63
4.1 Conclusion 63
4.2 Outlook 64
Reference 66

Chapter 1 Introduction

1.1 Background

The excessive consumption of fossil fuels such as natural gas, oil and coal has been contributed to the continuous accumulation of atmospheric CO_2, where the concentration of CO_2 in the atmosphere reached 412 ppm in2020.[1-4] CO_2 is a kind of greenhouse gas that leads to global warming and the deterioration of the environment. To solve these problems, many technologies have been developed to capture CO_2 from emission sources and utilize the CO_2 to produce chemical products, for example, urea and polycarbonates.[5, 6] The quantity of CO_2 emitted through fossil fuel utilization is considerably more than industrial requirements.[7] In recent years, carbon dioxide electrochemical reduction (CO_2ER) has become an attractive and promising approach to convert CO_2 into value-add chemicals and fuels (e.g. CO, HCOOH, CH_4OH, CH_4, etc.), driven by renewable energy.[8, 9] There are some intrinsic advantages in CO_2ER. Firstly, the chemicals consumed in this process are water and CO_2, and the electrolyte can be fully recycled. Secondly, produced high-energy-density fuels from this reaction, such as methanol and ethanol, can be directly used in vehicles, providing a promising strategy for stable and larger-scale renewable energy storage.[10] Thirdly, this conversion can be operated under mild conditions such as room temperature and/or ambient pressure[11], and the reaction system is relatively simple and modular, which can be easily scaled up for industrial applications.[12, 13]

1.2 Introduction of CO_2ER

Due to the strong binding energy of the C=O double bond (806 kJ mol^{-1}), CO_2 is considered a thermodynamically stable molecule.[14, 15] Therefore, the electrochemical reduction of CO_2 suffers from sluggish reaction kinetics.[16] Highly efficient electrocatalysts are essential to activate CO_2 molecules for further conversion and facilitate this reaction to obtain high activity, energy efficiency, and high selectivity for the target product. Based on the electrocatalyst used, CO_2ER can be generally classified as homogeneous catalysis and heterogeneous catalysis.[11, 16, 17]

1.2.1 Homogenous Catalysts

Homogeneous CO_2ER catalysts usually include transition metal coordination complexes with precise molecular structures.[14] These metal complex catalysts can be dissolved in electrolytes, and the interfacial electron is transferred from the supporting electrode to the reduced metal as the active centres, reacting with CO_2 and H^+ to form the intermediate products. With the final products detached from the active sites, the catalyst transforms into its original status for the next catalytic cycle (**Figure 1.1**).[11] Due to their special molecular structure and unique catalytic centres, homogeneous electrocatalysts exhibit high activity and selectivity toward CO_2ER. However, most of these metal complex catalysts have poor solubility, activity and stability in an aqueous environment and thus have to be applied in organic environments.[7] As a result, the high cost, toxicity and complicated post-separation are significant challenges in the homogenous CO_2ER process, which obstructs their widespread industrial application.[16]

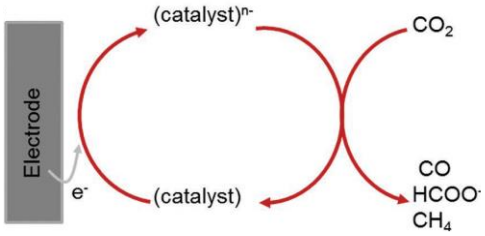

Figure 1.1. Scheme of a CO_2ER Homogeneous Electrocatalyst. Reproduced with permission.[11] Copyright 2018, John Wiley and Sons.

1.2.2 Heterogeneous Catalysts

On the other hand, the heterogeneous electroreduction of CO_2 is more desirable due to the facile synthesis of electrocatalysts, excellent performance and environmental friendliness. In addition, heterogeneous catalysts can be fabricated into a gas-diffusion type of electrolyzer, contributing to a higher current density of CO_2ER. It is promising for larger-scale applications in the industry.[18] In early studies, bulk and post-transition metals have been used as heterogeneous CO_2ER catalysts, and their intrinsic activities for CO_2ER also have been revealed. In recent decades, nanoscience and nanotechnology have made significant progress, contributing to the emergence of novel heterogeneous electrocatalysts, including nanostructured metals catalysts, metal-oxide-derived catalysts, heteroatom doped carbon materials and metal-organic frameworks. Compared to bulky catalysts, these new types of catalysts exhibit higher performance. However, the property of catalysts is still far from industrial demand due to the high fabrication cost, short lifetime, and low catalytic activity and selectivity.[16] Hence, robust, cheap, and efficient catalysts need to be developed.

1.2.2.1 Thermodynamics and Kinetics of Heterogeneous CO_2ER

The CO_2 electrolyzer, which is utilized for heterogenous CO_2ER, consists of a cathode, an anode, electrolytes, and an ion-exchange membrane. (**Figure 1.2**). The CO_2ER occurs at the cathode, while the oxygen evolution reaction (OER) occurs at the anode. The electrodes are put into electrolytes, which are usually a CO_2 saturated aqueous solution. An ion exchange membrane is required to avoid the products formed from the CO_2 reduction entering into the anode and further being oxidated, and only allows the movement of permeable ions.[16]

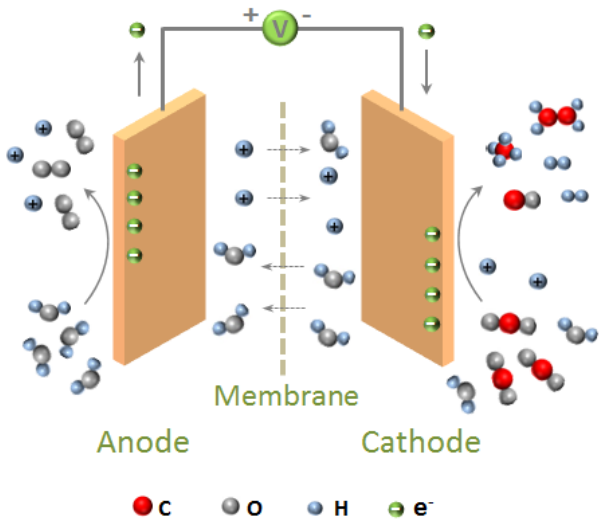

Figure 1.2 Schematic illustrates the electrolyzer for CO_2ER

The CO_2ER takes place at the surface or near the surface of heterogeneous catalysts.[13] This process involves multiple reaction steps and electron-proton transfers. Three main steps are involved in the CO_2ER process: i) chemical adsorption of CO_2 on the electrode; ii) electron transfer and/or proton migration to cleave C-O bonds and/or form C-H bonds; iii) configuration rearrangement of products for desorption from the electrode surface and diffuse into the electrolyte.[19] With the different electron-proton

transfer processes, CO_2ER can generate a variety of products, including CO, HCOOH or $HCOO^-$, CH_4, C_2H_4, CH_3OH, and C_2H_5OH. This not only makes the reaction kinetics complicated but also leads to poor product selectivity for CO_2 conversion.[13]

The thermodynamic electrochemical half-reactions of CO_2ER and the associate standard equilibrium potentials were listed in **Table 1.1**.[16] The equilibrium potentials of hydrogen evolution reaction (HER) (R1) are akin to CO_2 reduction. This coincides with an observed phenomenon that H_2 is a major side-product during the CO_2ER process. Also, there is only a small difference in the thermodynamic potential for different CO_2 reduction products (R2-R7). It is complicated to control the product selectivity during the reaction. The potential for activating CO_2 molecules to form a key intermediate species $CO_2^{\bullet-}$ (R8) is more negative than the other reactions (R2-R7). It indicates that a more negative potential compared to the equilibrium is needed to drive the CO_2 reduction to specific products.[20] The difference between these two potentials is identified as overpotential, and overpotential requires extra energy input for CO_2 conversion. Therefore, reducing the overpotential is highly desirable to improve energy efficiency. An efficient electrocatalyst is required to facilitate the formation of $CO_2^{\bullet-}$ by proton-assistance and multiple-electron transfer to reduce the high overpotential.

Additionally, the relationship between Gibbs free energy (ΔG) and potential (E^0) can be explained by the equation: $\Delta G = -zFE^0$, where z refers to number of electrons transferred, and F is the Faraday constant (96485 C mol^{-1}). According to this equation, the CO_2 electrochemical reduction with more positive E^0 is more favourable. Hence, the E^0 value in **Table 1.1** indicates that electrochemical reduction of CO_2 is more likely

to form the hydrocarbon or alcohol products rather than CO, HCOO, HCHO, and H_2 production. However, those results are not in accordance with the experimental results.[21] The reason is that the CO_2ER is influenced by the thermodynamic barrier and controlled by the kinetics of catalytic sites and accessible protons in the electrolyte. This means that the active site switches the electron and proton transfer to form preferable intermediates in the catalyst, which change the selectivity of CO_2ER.

Table 1.1 Standard potentials of CO_2 reduction reaction in aqueous solutions (V vs. SHE) at pH=7, 1.0 atm and 25°C.[16]

Half-electrochemical thermodynamic reactions	Equilibrium potentials (V vs. SHE) under standard conditions	Reference Code
$2H^+ + 2e^- \rightarrow H_2$	-0.42	[**R1**]
$CO_2 + 2H^+ + 2e^- \rightarrow HCOOH$	-0.61	[**R2**]
$CO_2 + 2H^+ + 2e^- \rightarrow CO + H_2O$	-0.52	[**R3**]
$CO_2 + 4H^+ + 4e^- \rightarrow HCHO + H_2O$	-0.51	[**R4**]
$CO_2 + 6H^+ + 6e^- \rightarrow CH_3OH + H_2O$	-0.38	[**R5**]
$CO_2 + 8H^+ + 8e^- \rightarrow CH_4 + 2H_2O$	-0.24	[**R6**]
$2CO_2 + 12H^+ + 12e^- \rightarrow C_2H_4 + 4H_2O$	-0.34	[**R7**]
$CO_2 + e^- \rightarrow CO_2^{\bullet -}$	-1.90	[**R8**]

1.2.2.2 Significant Index to Evaluate Heterogeneous CO_2ER

To estimate and compare the properties of various electrocatalysts, several essential parameters need to be clarified, including Faradic efficiency, current density, overpotential and Tafel slope.

Faradaic efficiency (FE) is an essential parameter for CO_2ER. It is the percentage of electrons consumed to manufacture a given product during a specific period. The FE

value can be calculated as the following equation: $\varepsilon_{Faradaic} = \alpha nF/Q$ where α is the number of electrons transferred (e.g., α = 6 for CO_2 reduction to CH_3OH), n is the number of moles for the desired product, F refers to Faraday's constant (96485 C mol^{-1}), and Q represents the total quantity of electrochemical charge. The FE of different CO_2ER production directly reflects the selectivity of electrocatalysts. Therefore, FE is the most significant parameter to estimate the property of electrocatalyst for CO_2ER.

Current density (j). The total current density for CO_2ER can be calculated by dividing the current by the geometric surface area of the working electrodes. The current density directly reflects the reaction rate. Because of the complicated CO_2ER products and competence of HER during the electrocatalytic process, the calculation of the partial current density for all CO_2ER products is necessary, which can be obtained by the equation: $j_{product} = FE_{product} \times j_{total}$.

Overpotential(η). The overpotential for the CO_2ER indicates the absolute magnitude of the difference between the potential required of generation of the product (E) and the equilibrium potential (E^0), $\eta = |E - E^0|$. Total energy utilization towards the CO_2ER products is determined by the overpotential and faradaic efficiency combined. The equation can estimate the energy efficiency (ε) of the CO_2ER, $\varepsilon = FE \times E^0/(E^0+\eta)$. This equation demonstrates that the low overpotential and high efficiency in the CO_2ER process can achieve high energy efficiency.

Tafel slope. The Tafel plot describes the relationship between the overpotential and the logarithm of the partial current density of the target product. The slope of the Tafel plot can be utilized to measure the reaction kinetics of the CO_2ER. Usually, when the slope

of the Tafel plot is 120 mV dec^{-1}, the reaction determining step (RDS) is a one-electron transfer to CO_2 to form $CO_2^{\bullet-}$ intermediate.[22] In contrast, when the slope of the Tafel plot is 59 mV dec^{-1}, the RDS was controlled by the one-electron transfer step and H^+ transfer.[23]

1.2.2.3 Challenges of Heterogeneous Catalysts

Many studies have been developed on the heterogeneous CO_2ER catalyst in recent decades, and significant progress has been achieved. However, there are few reports on the industrial applications of these catalysts. The reason is the limited performance of the CO_2ER, which is still far from industrial requirements (current density 200 mA/cm^2,[24] and stability >20,000 h[25]). The main problems and challenges in CO_2ER areas are summarised as follows.

Low energy efficiency. The enormous energy barrier for forming the critical intermediate $CO_2^{\bullet-}$ contributes to the requirement of a large overpotential. According to the energy efficiency's equation, a large overpotential results in low energy efficiency. The CO_2ER process's proton supply is from the water electrolysis. As the equilibrium of potential hydrogen evolution reaction (HER) is also similar to CO_2ER, the CO_2ER competes with the HER during the reduction process, leading to a higher energy requirement with lower energy efficiency.

Poor selectivity. The similar equilibrium potentials of the half-reactions result in poor selectivity with the mixed products from CO_2ER containing various gaseous and liquid species. The high cost for separating multiple products makes developing catalysts with

single-selectivity highly desirable.

Low current density. Due to the sluggish kinetics of CO_2 reduction and low solubility of CO_2 in aqueous electrolytes, the reactant diffusion obviously limited current density from exceeding 30 mA/cm^2. This is far from the technical requirements for practical applications.[24]

Short lifetime. The surface composition and structure of electrocatalysts have profound impacts on the CO_2ER. The surface structures of the catalyst are rearranged, and the surface is contaminated during the electrolytic process. This leads to a variety of side effects that deactivate the catalysts. In addition, reaction intermediates, by-products and/or contaminants in the electrolyte can block the diffusion channels, which also slows down the reaction process. All of these factors severely influence the stability of the catalysts.[26] To date, the reported lifetime of catalysts are less than the 100 hours required for industrial application.

Therefore, a promising heterogeneous CO_2ER electrocatalyst should achieve high energy efficiency at the CO_2ER process, high current density, high selectivity, and long-term stability at low overpotentials.

1.3 Current Heterogeneous Catalysts for CO_2ER

Heterogeneous CO_2ER have been an attractive research area during the last few decades, and many electrocatalysts have been developed. Up to now, five types of materials demonstrate high performance toward CO_2ER; metal, metal oxides, transition-metal dichalcogenides, metal-free carbon materials, and single-atom

catalysts. In this section, the representative catalysts have been discussed and tabulated to give a general overview of catalyst development. The influence of porous structure on catalytic performance will be addressed in the next section.

1.3.1 Metal Catalyst

1.3.1.1 Bulk Metals Catalyst

In the early studies, the bulk transition and post-transition metals were directly utilized as the CO_2ER catalysts. The properties of bulk metals control the formation of CO_2 reduction products. For example, the main products of Cu are hydrocarbon compounds (CH_4 and C_2H_4).[27-29] Zn metal demonstrates excellent selectivity toward CO, while the major reduction product for Sn is HCOOH. [30, 31]Hori and his co-workers indicate that these bulk metal catalysts can be divided into four groups based on the reduction products.[31] Group 1 contains Pb, Hg, In, Cd, Bi and Tl, producing the formate ($HCOO^-$) or formate acid (HCOOH) as the major product. Au, Ag, Zn, Pd belong to Group 2, giving CO as the major product. Group 3 only includes Cu, producing hydrocarbons such as CH_4, C_2H_4, C_2H_6. Ni, Fe, Pt and Ti belong to Group 4, where HER occurs dominantly.[16]

The ability of these metals to bind the different intermediates determine the selectivity of the reduction products. (shown in **Figure 1.3**).[16] The major CO_2ER product of Group 1 metals is formate or formic acid. These metals can hardly stabilize formed $CO_2^{\bullet-}$ intermediates; thus, formate or formic acid have to be obtained through an outer-sphere mechanism.[32] The metals in the other group can stabilize the $CO_2^{\bullet-}$ and convert them to

*COOH and *CO intermediates. The metal in group 2 cannot stabilize the *CO intermediates. Thus, CO is readily desorbed from the metal surface and emerges as a predominant product. For Group 4, the *CO is bound too strongly on the metal surface, which results in catalyst poisoning and further hinders the reduction of the *CO intermediates. In comparison, The *CO and *COOH intermediate properly adsorbed on the surface of Cu and allows further conversion to high-order carbon products such as CH_4 and CH_3OH via *COH or *CHO intermediates.[16]

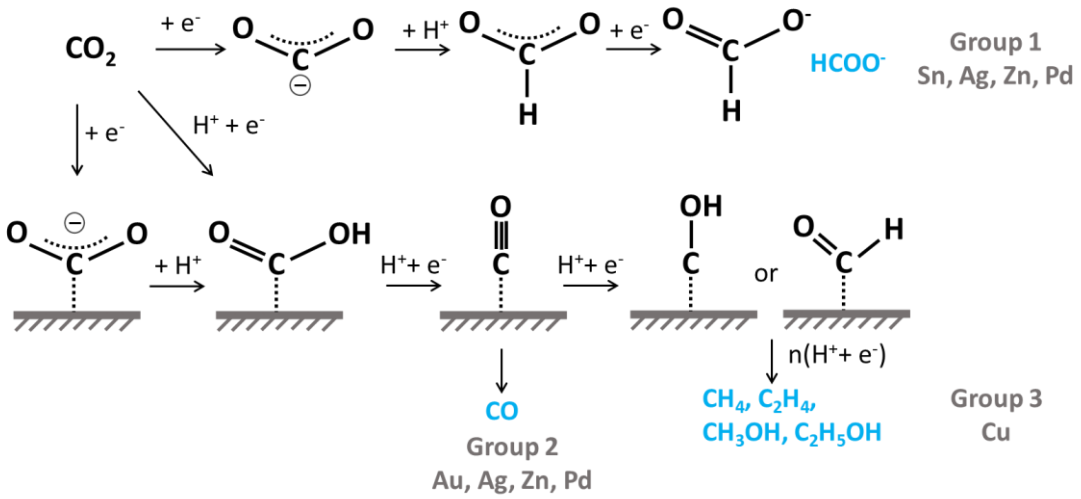

Figure 1.3 Possible reaction mechanism of electrochemical CO_2 reduction on various metal electrodes in aqueous solutions. Redrawn according to reference.[16] Copyright 2018, John Wiley and Sons.

However, the observation of the surficial chemistry process on the transition metal electrode during the CO_2ER is more complicated.[16] According to Kuhl et al.[33], methane and methanol were observed when the heterogenous catalyst was Ag, Zn, Cu, Ni, and Pt. Also, only methane was formed on Fe, while the Au surface produced methanol. Hence, they reported the selectivity of CO_2ER for Fe and Au was controlled by the CO binding strength and depended on the different oxophilicites between Au and Fe. Due

to the strong Fe binding affinity for O, the second C-O bond of CO_2 could be broken, which continue the generation of methane. On the other hand, due to the weakly Au binding affinity for O, the Au keeps the second C-O bond active to generate methanol. Thus, this idea can be utilized to design the catalyst to produce hydrocarbon or alcohol.

The bulky metallic catalysts demonstrate attractive properties toward CO_2ER. However, the performance of bulk metals is still far from meeting industrial requirements when considering selectivity, activity and stability.[7] Also, due to the limitation of characterization techniques and catalyst synthesis methods in the early studies, the information on reaction rate and stability is inadequate. Additionally, the morphology, structure, and chemical composition of the metallic surface are complicated, which hinder the understanding of the mechanism for CO_2ER.[30]

1.3.1.2 Nanostructured Metals

The last decade has witnessed considerable progress in nanoscience and nanotechnology. The catalyst of CO_2ER also focused on nanostructured materials. Compared with bulk metals, nanostructured metals have several intrinsic advantages.[34] First, the exposed active sites of the nanostructured metals are more than bulk metals due to the large specific surface areas, which enhances the reaction rate and improves the tolerance to impurities in the electrolytes. Additionally, from both experiments and theoretical aspects, the morphology, crystal facets, roughness, and particle size of the nanostructure metal catalyst significantly influence the activity and selectivity toward CO_2ER.[35, 36] At present, the nanostructured Au, Ag, Cu, Zn, Pd, Co, In, Bi, and Sn have

been widely investigated as electrocatalysts for CO_2ER, and exhibit better performance than their bulk counterparts.[7]

1.3.1.3 Metal Alloys Catalysts

As mentioned above, the binding strength of the key intermediate (e.g. *COOH, *CO) on the surface of metals determine the activity and product selectivity of the CO_2ER. The binding strength of the key intermediate can be regulated by introducing other metals into the metallic catalyst, which can improve the properties of CO_2ER significantly.[37] Only Cu has been reported to properly connect the key *CO intermediate for further conversion to high-value products such as ethylene, methanol, ethanol, etc.[30] However, it will result in multiple products. Therefore, Cu alloying with other metals were developed to optimize the selectivity procedure by tailoring *CO and * COOH's binding strength on the Cu surface, e.g. Ni, Sn, Pb, Cd, Au, and In. Apart from Cu based alloys, the non-copper alloys (e.g. Pd-Au, Pd-Sn, Au-Fe) also exhibit good activity and selectivity for the CO_2ER. **Table 1.3** summarises some representative alloy catalysts for the CO_2ER, providing insights into designing this kind of catalysts.

Table 1.2 Performance for alloy catalysts toward CO_2ER. Modified according to referenc[7]

Alloys	**Electrolyte**	**product**	**$E_{vs.RHE}$**	**$j_{partial}$ (mA/cm^2)**
$CuAu_3$	0.1M $NaHCO_3$	CO (65)	-0.73	230A g^{-1}
$Cu_{11}In_9$	0.1M $NaHCO_3$	CO (95)	-0.6	0.6
Cu_2Cd	0.1M $KHCO_3$	CO (84)	-0.1	8.0
Cu-Sn	0.1M $KHCO_3$	CO (90)	-0.6	1.0
Cu_3Pd_7	0.1M $KHCO_3$	CO (80)	-0.8	0.5
Cu_3Pt	0.5M $NaHCO_3$	Methane (21)	-0.93	NA
$Cu_{64}Au_{36}$	0.5M $NaHCO_3$	Ethanol (12) Methanol (15.9)	-0.41	NA
Cu-Pd	1M KOH	Ethylene (47) Ethanol (15)	-0.74	NA
Cu-Ag	1M KOH	Ethylene (60) Ethanol (25)	-0.7	NA
Cu-Ag	0.5M $KHCO_3$	acetic acid (21.2)	-1.33	NA
Cu_4Zn	0.1M $KHCO_3$	Ethanol (29.1)	-1.05	8.2
$Cu_{0.2}Sn_{0.8}$	0.5M $KHCO_3$	$HCOO^-$ (85)	-0.35	3
Au-Fe	0.5M KHCO	CO (97.6)	-0.4	11.1
$Au_{55}Pd_{45}$	0.1M $KHCO_3$	$HCOO^-$ (10)	-1.0	0.3
$Ag_{76}Sn_{24}$	0.5M $NaHCO_3$	CO (80)	-0.8	16.0
$In_{90}Sn_{10}$	0.1M $KHCO_3$	$HCOO^-$ (92)	-1.2	13.8
Pd-Sn	0.5 $KHCO_3$	$HCOO^-$ (99)	-0.43	1.8
Mo-Bi	0.5M [EMIM]BF_4 MeCN	Ethanol (71.2)	-0.7vs SHE	12.1

1.3.2 Metal Oxides

Compared with metallic catalysts, the fully or partially oxidized compounds can impact the binding strength of *CO and *COOH intermediate on the active site. Hence, the presence of oxidized metals can improve the selectivity and activity at the CO_2ER process. However, only a few metal oxides such as TiO_2, FeO_x and Cu_2O exhibit the electrocatalytic activity toward CO_2ER.[38-41] The reason is that most metal oxide (e.g. CuxO, SnOx and ZnO) may be rapidly reduced to metals under negative potentials in neutral or near-neutral electrolytes. Ma et al.[42] synthesized a TiO_2 supported Ag NPs catalyst for CO_2ER, demonstrating remarkable performance (FE_{CO} > 90% and j_{CO}> 100mA cm^{-2}) in aqueous solutions. Furthermore, the author indicated that the key reaction intermediate $CO_2^{\bullet-}$ was stabilized by the Ti^{4+}/Ti^{3+} redox couple, enhancing the performance of TiO_2 supported Ag NPs catalyst **(Figure 1.4**).

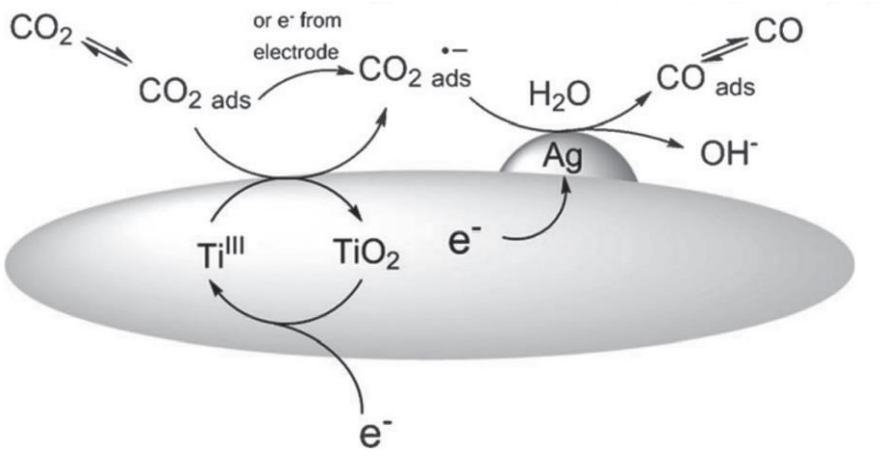

Figure 1.4 Schematic illustration for the proposed pathway of the CO_2 reduction to CO on the TiO_2 supported Ag NPs. Reproduced with permission.[42] Copyright 2014, John Wiley and Sons.

Additionally, some metal oxides also demonstrate good electrocatalytic

performance toward CO_2 in organic solution or ionic liquids. For instance, Ramesha and Kamat et al.[43] reported that the nanostructured TiO_2 converted CO_2 into methanol with high faradic efficiency of ~ 90% in 0.1 M TEAP /acetonitrile (0.33 M H_2O). Furthermore, Chu et al.[44] found that the CO_2 can be converted into low-density polyethylene (LDPE) by nanostructured TiO_2 film in the 1-enthyl-3-methylimidazolium tetrafluoroborate ([EMIM]BF_4) aqueous solution.

1.3.3 Transition-Metal Dichalcogenide Catalysts

Compared with the nanostructured metal and metal oxide catalysts, the nanostructured transition metals dichalcogenides (TMDs) have obtained significant attention in electrocatalysis due to their low cost, 2D layered structure, prominent active sites and defect-rich surface.[45-48] However, there are only a few reports about the usage of TMDs for CO_2ER. In 2014, Yamaguchi and co-workers[49] first synthesized FeS and Ni-containing FeS by a hydrothermal method and the obtained catalysts were estimated for CO_2ER in a diluted acidic solution. They pointed out that the bared FeS demonstrate a relatively weak capacity to reduce CO_2 so that the NH_3 and Ni were used to regulate FeS to achieve CO_2 into CO, CH_4 and formate.

Asadi et al.[47] indicated that layer-stacked bulk molybdenum disulphide (MoS_2) with Mo-terminated edges was utilized as an efficient electrocatalyst to convert CO_2 into CO in ionic liquid [EMIM]BF_4-H_2O electrolyte, which demonstrated remarkable electrocatalytic activity and product selectivity (65 mA cm^{-2}, FECO~98% at -0.764V vs. RHE), as shown in (**Figure 1.5** a-d) According to the Density functional theory

(DFT) calculation, the high d-electron density on the MoS_2 and metal-like low work function contributed to the excellent properties of MoS_2 catalyst. Hence, the vertically aligned MoS_2 with additional Mo atoms on the edges as active sites (**Figure 1.5** e) were obtained to prove the DFT results. As expected, the vertically aligned (VA) MoS_2 reaction rate increased (130 mA cm^{-2} at -0.764 V vs. RHE), corresponding with DFT results. Additionally, the author proposed that ionic liquid [EMIM]BF_4-H_2O electrolyte enhanced the CO_2 transfer to the catalyst surface by the complexation under the acidic condition to enrich local CO_2 concentration. Also, the reaction barrier of electrons passing into CO_2 can be lowered.

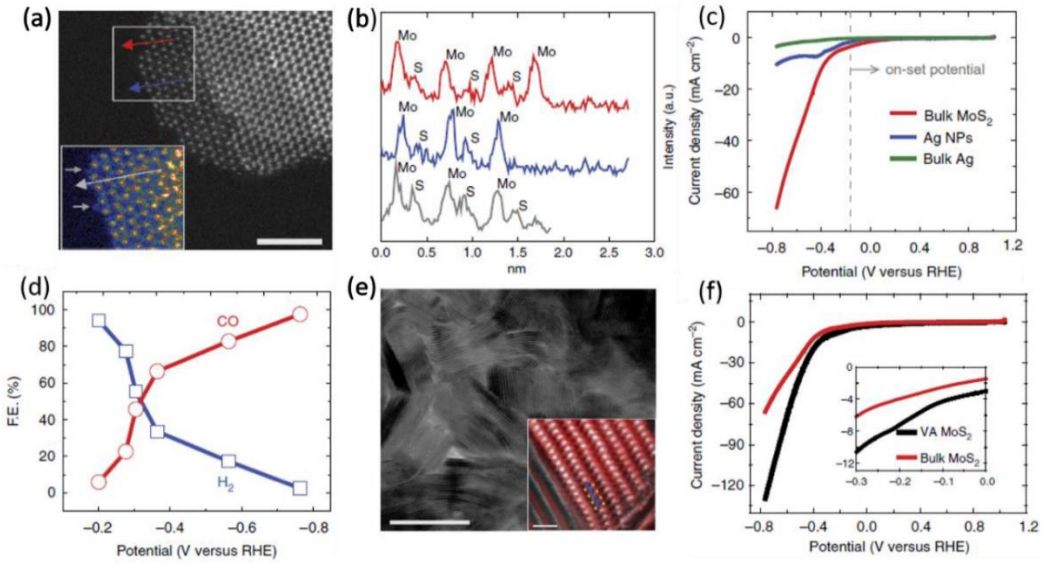

Figure 1.5 (a)HAADF image and LAADF image (inset) for MoS_2 edges (scale bar, 5 nm) (b) The line scans for MoS_2 to prove the Mo atom as ending ; (c) LSV curves of bulk Ag (green line), Ag NPs (blue line), and bulk MoS_2 (green line) (d) FE_{CO} and FE_{H2} for bulk MoS_2; (e) Annual bright-field STEM (VA MoS_2 scale bar,20nm), and inset image is STEM for VA MoS_2 (scale bar 50nm); (f) bulk MoS_2 and VA MoS_2 nanosheets CO_2ER performance. Adapted with permission.[47] Copyright 2014, Nature

Publishing Group.

1.3.4 Metal-Free Carbon Catalysts

In recent times, metal-free carbon-based catalysts have received a lot of attention as CO_2 electrocatalysts due to their intrinsic advantages, such as high surface area, high conductivity, excellent chemical stability, and remarkable mechanical strength, which may enhance the CO_2 electroreduction. Moreover, carbon materials are cheap and environmentally friendly and abundant in the environment. Furthermore, carbon atoms can form different dimensions and structures,[50] such as zero-dimensional (0D) carbon nanodots, one-dimensional (1D) carbon nanofibers(CNFs), two-dimensional (2D) graphene and three dimensional (3D) diamond.[51] Amongst bulky or nanostructured carbon materials do not have enough catalytic activity to CO_2ER since the essential $CO_2^{\bullet-}$ intermediate is weakly absorbed on electroneutral carbon atoms.[15] However, one of the critical highlights of carbon materials is that doped heteroatoms (e.g. B, N, P, and S) can simply alter their crystallizations and electronic structures, which would enhance the CO_2ER properties.[16]

The crystalline structure of carbon impacts the electrocatalytic activity and product selectivity. Relevant reaction mechanisms indicate that the carbon's binding ability to key intermediates was determined by the carbon allotropes, contributing to product selectivity. Also, the porosity of the carbon-based catalyst would enhance the CO_2 diffusion and ion transfer. The different pore sizes of carbon-based catalysts demonstrate different properties. For example, the micropores increase the

electrochemical surface areas and the active sites, and the mesopores enhance ion transfer.[52]

In 2013, Kumar et al.[53] firstly utilized the synthesized polyacrylonitrile-derived N-doped carbon nanofibers (CNFs) as an effective electrocatalyst to convert CO_2 into CO in [EMIM]BF_4-H_2O electrolyte. This catalyst demonstrated excellent catalytic activity. For example, under identical testing circumstances, the current density of the catalyst was approximately 13 times and 4 times higher than bulk Ag film and 5 nm Ag NPs (**Figure 1.6** (a)-(d)). The XPS results indicated that the position of the pyridinic N atom remained the same after the reaction. Hence, the catalytic activity of CNFs was attributed to the positively charged carbon atoms adjacent to the pyridinic N. The reaction mechanism was explained in **Figure 1.6** (e)**.** In the first step, the naturally oxidized carbon atoms captured electrons and were reduced by the redox cycling process. Secondly, the reduced carbon attracted [EMIM-CO_2] complex intermediates and transferred electrons to the intermediates. Then the reduced carbon atoms returned to their original state. Finally, the produced CO was released from $[EMIM]^-$ complex

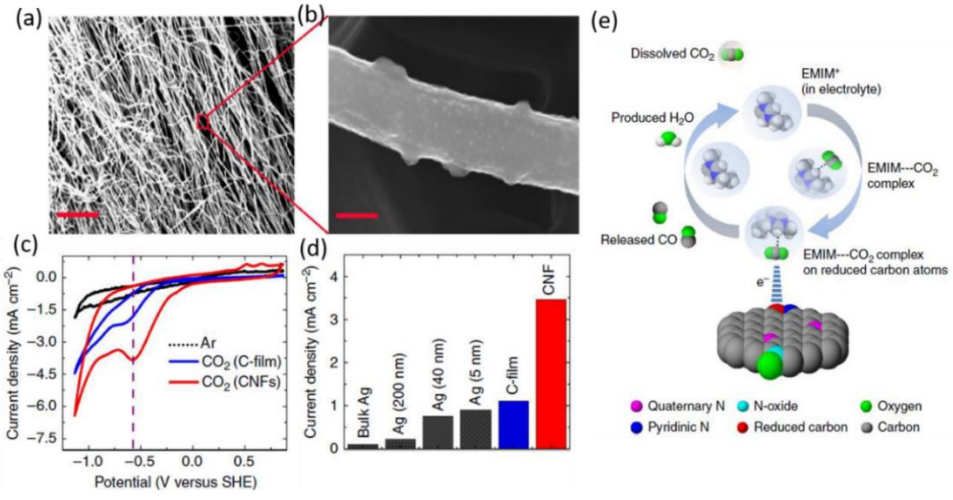

Figure 1.6 (a), (b) SEM images for N-CNFs; (c) CVs curves for carbon electrode and

CNTs electrode in pure EMIM-BF_4 electrolyte with Ar and CO_2 saturated. (d) The current density for CO_2ER at different electrodes in CO_2 saturated pure EMIM-BF_4 electrolyte. (e) Schematic illustration of the CO_2ER mechanism for N-CNFs. Reproduced with permission.[53] Copyright 2013, Nature Publishing Group.

Apart from N-doping, B dopant for carbon-based is also an efficient method to modify carbon electronic structure and to improve the electrocatalytic activity of caron materials. Sreekanth and co-workers[54] reported that B-doped graphene (B-GO) was employed as an electrocatalyst for CO_2ER. The B-GO was prepared by the uniform mixture of the GO and boric acid powder placed in the tube furnace and heat 900 ^oC at Ar atmosphere. LSV curve of B-GO and graphene in CO_2-saturated 0.1 M $KHCO_3$ solution indicated that B-GO's current density increases dramatically, proving the electrocatalytic activity of B-GO. The FE of formate for B-GO was 66% at -1.4 V vs SER, which was better than bismuth (Bi) catalyst at the same experimental condition. XPS spectrum indicated that B atoms from three species in the hexagonal graphene, including BC_3 at 189.4 eV, BC_2O at 190.5 eV, BCO_2 at 191.9 eV, respectively. According to DFT calculation, the presence of B atoms contributed to the asymmetric spin density in the graphene framework as the possible pathway for CO_2-to-formate conversion.

The performances for several metal-free carbon catalysts are summarized in **Table 1.3**. According to this table and the previous discussion, the carbon structures and doped-heteroatom determine the performance of the metal-free carbon catalysts. However, these metal-free carbon catalysts have low activity. Doping single transition

metals in the N-doped carbon is an efficient way to boot the CO_2ER performance

Table 1.3 Summary of the properties for metal-free carbon catalysts toward CO_2ER from recently reports.

Heteroatoms	Carbon material	Electrolyte	Product (FE%)	$E_{vs.RHE}$	$j_{partial}$ mA cm^{-2}
N	CNT[55]	0.5M $NaHCO_3$	CO (90)	-0.9	~5.5
N	Porous C[56]	0.5M $NaHCO_3$	CO (83.7)	-0.82	~8
N	Graphene like carbon[57]	BMMI-BF_4	CH_4 (91.8)	-1.4 vs. SHE	~1.4
N	CNFs[53]	[EMIM]BF_4	CO (98)	-0.573	3.5
N	CNT[58]	0.1M $NaHCO_3$	$HCOO^-$ (81)	-0.9	~3.8
N	MWCNT[59]	0.1M $KHCO_3$	CO (80)	-0.39	0.75
N	Graphene foam[60]	0.1M $KHCO_3$	CO (85)	-0.58	1.9
N	GQDs[61]	1M KOH	Ethylene (31) Ethanol (14)	-0.75	~40
N	diamond[62]	0.5M $NaHCO_3$	Acetate (71)	-0.8	~6.2
N	graphene[63]	0.5M $KHCO_3$	HCOOH (73)	-0.84	7.5
B	dimond[64]	1M CH_3OH	HCHO (74)	-1.7 vs Ag/Ag^+	NA
B	graphene[54]	0.1M $KHCO_3$	$HCOO^-$ (66)	-0.14	NA
B, N	diamond[65]	0.1M $KHCO_3$	Ethanol (93.2)	-1.0	NA
F	Carbon[66]	0.1M $NaClO_4$	CO (89.6)	-0.62	0.24

1.3.5 Single-Atom Catalysts

Single-atom catalysts indicate that active metal sites are atomically dispersed on or embedded in supporting materials. Recently, single-atom catalysts have become more

attractive due to its impressive catalytic activity for CO_2ER. The single-atom sites were considered as a curial role in CO_2 molecules adsorption and activation. The single-atom catalysts could be synthesized by various approaches, such as pyrolysis, wet chemistry synthesis, physical and chemical vapour deposition, electrochemical deposition, etc.[11, 67-71] Compared with other catalysts, the single-atom catalyst would enhance the exposure of the active sites to the CO_2 and proton, which improve the catalytic property. Specifically, single-atom metal-nitrogen carbon (M-N-C) catalyst is promising for the CO_2ER due to its high selectivity and low cost. It contains the transition metal-nitrogen structure (M-N, such as Fe-N, Co-N and Ni-N), which are active sites for converting CO_2 into CO. Here, some representative M-N-C single-atom catalysts will be introduced in this section.

In 2015, Strasser et al.[72] firstly synthesized the atomical transition metal dispersed on Nitrogen-doped carbon catalysts for CO_2ER. The Fe-N-C, Mn-N-C, Fe Mn-N-C were synthesized by processing the Fe and Mn chloride salts, polyaniline and commercial carbon blacks using pyrolysis and acid leaching. These catalysts exhibited excellent catalytical activity and high selectivity toward CO_2ER. They indicated that the CO was produced on the M-N_x moieties, unrelated to the type of metal dopants. The binding strength of CO on metal centres was relatively strong, which facilitated the protonation of CO and the generation of CH_4

Ju and co-workers[73] explored a series of transition metals (Mn, Fe, Co, Ni and Cu) on nitrogen-doped carbon for CO_2ER, and the result was shown in **Figure1.7**. The Fe-N-C catalyst exhibited high CO faradic efficiency at a low potential. The Ni-N-C

catalyst was very active and highly selective for CO_2 to CO conversion at high potentials. In contrast, the catalytic activity of the Co-N-C catalyst was the worst compared to the other catalysts. Additionally, small amounts of CH_4 were observed in the Fe and Mn catalyst. Although the number of surface-active sites was low, the CO partial currents (product rate) of Ni-N-C were comparable to that of Au-based catalysts. They proposed that this family of transition metal nitrogen-doped carbon catalysts can be utilized in the electrochemical production of CO from CO_2

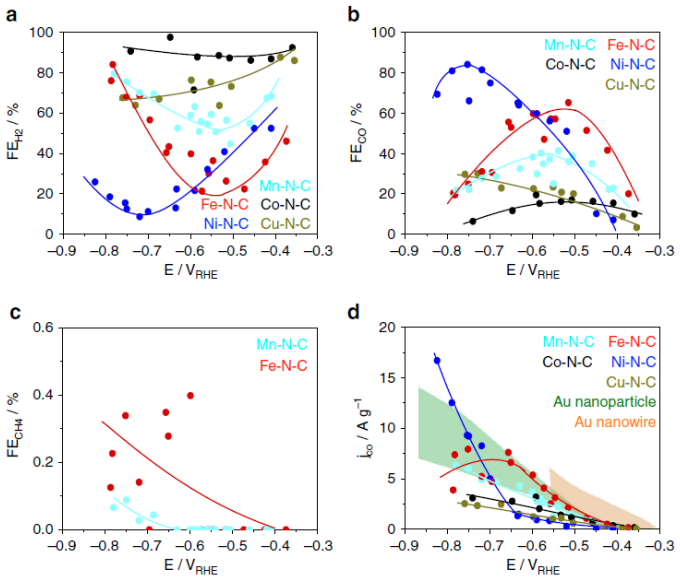

Figure 1.7 a-c) Faradic Efficient (FE) for H_2, CO, and CH_4 at the different applied potential with IR-corrected. d) Catalyst mass-normalized CO partial current for five types of M-N-C catalysts, which were compared with the Au catalysts (properties ranges for Au-nanoparticles and Au-nanowires are represented by filled regions) reproduced with permission.[73] Copyright 2017, Nature Publishing Group.

Different N-C precursors and synthesis pathways can be utilized to obtain the Fe-N-C, Ni-N-C and Co-N-C single-atom catalysts. All of these catalysts demonstrate outstanding properties for CO_2 to CO conversion, and the performance of some

representative metal-nitrogen doped carbon catalysts are shown in **Table 1.4**. Zhao and co-workers[74] obtained atomic nickel atoms and nitrogen-doped porous carbon catalysts by the pyrolysis of the precursor Ni-ZIF-8 at 1000 ℃ in Ar. The Ni-ZIF-8 was produced by adding the Ni^{2+} ion solution into ZIF-8 homogenous n-hexane solution, and the Ni^{2+} ions were absorbed and fixed in the ZIF-8 pores. The extended X-ray absorption fine structure (EXAFS) and X-ray absorption near-edge structure (XANES) demonstrated that Ni atoms connect with three N atoms, which proved the formation of the Ni-N_3 structure. This catalyst exhibited good performance for the CO_2 to CO conversion. The catalyst achieved the 71.9 %FE of CO at -0.9 V vs. RHE with the CO current density of 7.37 mA cm^{-2}.

As mentioned above, the Fe-N-C achieved superior activity and selectivity for CO_2ER at a lower potential. Huan and CO-workers[75] produced Fe-N-C single-atom catalysts via pyrolysis of Fe-ZIF-8 precursor. Their EXAFS and Mössbauer absorption spectroscopy results revealed that the Fe atom connected with four N atoms without the Fe-Fe bond, proving the successful formation of the Fe-N_4 structure. This catalyst demonstrated remarkable CO_2ER properties, which reached the high selectivity with a maximum CO FE of 91% at -0.6 V vs. RHE. However, the current density of this catalyst was only 7.5 mA cm^{-2} in 0.1 $NaHCO_3$.

In addition, the GO would be utilized as the carbon precursors for Fe-N-C single-atom catalyst. Zhang et al.[76] selected GO with the various oxygen-containing functional groups (e.g. epoxy, hydroxyl, carboxyl and carbonyl groups) as the carbon precursors to synthesize the Fe-N-C. The GO absorbed the optimized level of 0.52 wt% Fe^{3+} ions

by electrostatic interactions. Then the Fe-GO was heated in a high-temperature range (650-800 ℃) under an Ar/NH_3 atmosphere for one hour. After these steps, a Fe-N bond was formed in the graphene framework. Their EXAFS spectra results indicated that the Fe atoms bonded with four nitrogen to form the Fe-N_4 sites. However, the Fe-Fe bonds were detected in the catalyst due to the limitations of their synthesis procedures. Despite the presence of Fe-Fe, a large number of the Fe-N_4 sites (active sites) contributed to the excellent CO_2ER properties. The DFT results indicated the presence of a synergetic impact between Fe-N_4 species and N doping contributed to the decrease in the energy barrier for the generation of COOH*. Hence, Fe-N_4 boosted the CO_2ER performance.

Additionally, the active state and structure of Fe and N species in the Fe-N-C catalyst would impact the performance of CO_2ER. Gu[77] used the Fe(II)-ZIF-8 and Fe(III)-ZIF-8 to synthesize the Fe-N-C catalyst. They examined the active state of iron and nitrogen species in the Fe-N-C single-atom catalysts by an *operando* XAS technique. Their Fe K-edge XANES spectra revealed an energy shift in the Fe K-edge from -0.4 to -0.5V vs. RHE, which was related to the Fe element's 2+/3+ redox transition. They suggested the activity of Fe^{3+}-N-C is higher than Fe^{2+}-N-C due to the improvement of CO_2 adsorption and CO desorption on the Fe^{3+} ion. They also proposed that the pyrrolic N species were the optimum N state for stabilizing Fe^{3+} ions in carbon substrate. They also applied the Fe^{3+}N-C catalyst into the flow cell, and the catalyst achieved excellent CO_2ER performance (CO FE of 90% and j_{co} of 94 mA cm^{-2} at a low potential -0.45 V vs. RHE). Their work proved CO_2ER is a promising technology for industrial application, and the Fe^{3+}-N-C was a potential electrocatalyst for a scale-up

commercial utilization.

At present, high-temperature pyrolysis is a fundamental method to acquire M-N-C single-atom catalysts. Sintering of the precursor occurs uncontrollably, resulting in mixed M-N_x species and metallic aggregates.[78] This results in the decrease of the density for M-N_x and deteriorates the performance of the catalyst toward CO_2ER due to the exitance of HER-active sites (e.g. metal clusters or nanoparticles). To avoid the generation of HER-active metal nanoparticles, the metal loading in M-N-C materials is normally low, which negatively impacts the productivity of CO_2 conversion. Therefore, increasing the density of M-N sites on carbon materials is highly desirable to promote the catalytic performance for CO_2ER. Additionally, the M-N_x sites exposed for proton and CO_2 is quite limited. The precursors inevitably undergo partial fusion and aggregation. As a result, a number of the active sites are non-uniformly dispersed and sealed within the internal carbon matrix, which hinders the mass transfer to the M-N-sites.[79]

Table 1.4 Summary of the properties of single-atoms catalysts for CO_2ER toward CO

Single-atom	**N-C precursor**	**Electrolyte**	**FE**/%	$\mathbf{E}_{vs.RHE}$	$j_{partial}$ ($mAcm^{-2}$)
Fe-N-C[72]	PANI	0.1M $KHCO_3$	80	-0.5	~3 A g^{-1}
Fe-N-C[73]	4,4'-Dipyridyl	0.1M $KHCO_3$	65	-0.55	~3.8A g^{-1}
Fe-N-C[80]	ZIF-7, NH_3	0.1M $KHCO_3$	85	-0.43	~ 8
FeN_x-CNT[81]	Melamine, CB	0.1M Na_2SO_4	85	-0.6	NA
FeN_4-C[75]	ZIF-8	0.5M $NaHCO_3$	90	-0.6	5.4

Fe-N-CNT/CNS[82]	FePc, CNT	0.1M $KHCO_3$	69	-0.59	0.82
Fe-N-C nanofibers [80]	PAN, NH_3	0.1M $KHCO_3$	95	-0.53	4.71
Fe^{3+}-N-C[77]	ZIF-8	0.5M $KHCO_3$	90	-0.45	94 (flow cell)
Ni single atom[74]	ZIF-8	0.1M $KHCO_3$	70	-1.0	7.37
Ni-N-C[73]	4,4'-Dipyridly	0.1M $KHCO_3$	85	-0.78	~12.5 A g^{-1}
Ni-N_4-C[83]	g-C_3N_4, glucose	0.5M $KHCO_3$	99	-0.81	28.6
Ni atoms on graphene[84]	GO, NH_3	0.5M $KHCO_3$	95	-0.73	11
Ni-single atoms[85]	Amino acid melamine, GO	0.5M $KHCO_3$	95	-0.72	22
Ni-N-graphene[86]	Pentaethylene-hexamine, GO	0.1M $KHCO_3$	90	-0.7	NA
C-Zn_1Ni_4 ZIF-8[87]	ZIF-8	0.5M $KHCO_3$	92	-0.53	~15
Ni^{2+}@N-G[88]	g-C_3N_4 glucose	0.5M $KHCO_3$	92	-0.68	9.38
Co-N_2-C[89]	ZIF-8	0.5M $KHCO_3$	94	-0.63	18.1
Co-N_5-C[90]	Melamine-polymer, CoPc	0.2M $NaHCO_3$	99	-0.73	6.2
Co-N-C[91]	CTF	0.1M $KHCO_3$	85	-0.7	~1

1.4 Importance of Porous Structure

The mass transfer and kinetics of CO_2ER are dependent on the morphology and porosity of the catalyst. Therefore, the activity and selectivity of the electrocatalyst for the CO_2ER may be influenced by the catalyst morphology.[92, 93] Hossain et al.[94] employed the nanoporous Au as the electrocatalyst for CO_2ER. The nanoporous Au was obtained by alloying/dealloying and acid washing. They investigated three types of catalysts: simple polycrystalline Au, Au alloyed with zinc (NP-Au-Zn), and nanoporous

Au. They pointed out that NP-Au-Zn and nanoporous Au both possess an interconnected network of porosity. The pore sizes of NP-Au-Zn was ranging from 250 to 500 nm, while the nanoporous Au was 750 to 1000 nm. The test results indicated that the primary product of polycrystalline Au was H_2 because of few active sites on the plane surface. The NP-Au-Zn and nanoporous Au both achieved high FE of CO with NP-Au-Zn ~ 90% and nanoporous Au ~ 95%. However, the nanoporous Au demonstrated excellent catalytic activity; the production rate of the nanoporous Au was ~300 μmole cm^{-2} h^{-1}, which was 3 times higher than NP-Au-Zn and 65 times higher than that of polycrystalline Au. ECSA of the NP-Au-Zn was calculated as 1.59 $cm^{2,}$ and nanoporous Au was calculated as 2.54 cm^2, and they proposed that the increase of the catalytic activity was dependent on the extent of surfaces area. The pore size of nanoporous Au was too large (> 750 nm), which cannot provide the information of the pore size influence for catalytic selectivity. But it was noted the existence of porosity enhances the catalytic activity toward CO_2ER.

In addition, the pore size of the catalyst impacts the reduction condition of the CO_2ER. The mesoporosity affects the transfer of CO_2 and proton, which contributes to the pH gradient generation in the local surrounding area. Daiyan et al.[95] reported that the mesoporous tin oxide catalyst achieved superior selectivity for converting CO_2 into formate at a low overpotential. The mesoporous SnO_2 was synthesized via the nano-coating method utilizing the KIT-6 as the hard template, as shown in **Figure 1.8** A. The TEM image revealed that the m-SnO_2 possessed an ordered structure that was the same as the three-dimensional structure of the KIT-6 template (**Figure 1.8** B). Also, the TEM

showed the pore size of the m-SnO_2 was 4 nm, proven by the Barre-Joyner-Halenda method (**Figure 1.8** C). They investigated the performance of the m-SnO_2 toward CO_2ER in 0.1 M $KHCO_3$, and the SnO_2 nanoparticles (SnO_2 NPs) and Sn nanoparticles supported on carbon black (SnO_2/C NPs) were employed as controls. The m-SnO_2 demonstrated the better selectivity toward $HCOO^-$ generation, achieving the maximum FE_{HCOO-} of 75% at an applied potential of -1.15 V. Additionally, the m-SnO_2 catalysts can convert CO_2 into formate within wide potential windows (from -0.75 to -1.25V) where the FE_{COOH-} of m-SnO_2 was consistently above 50%. In contrast, the SnO_2 NPs suffered from sluggish reaction kinetics and attained a mere FE_{HCOO-} of 20% at -1.05V. The FE_{HCOO-} for SnO_2 NPs also increased at a higher overpotential but the FE_{HCOO-} was still lower (~52%) (**Figure 1.8** D). Compared with SnO_2, the SnO_2/C NPs exhibited higher catalytic activity and better selectivity for the formation of formate. They also proposed that the carbon black enhanced the conductivity of the catalyst, improving the activity toward CO_2ER, and the formation of Sn-C carbon boosted the selectivity of the catalyst (**Figure 1.8** E). Hence, the mesoporous structure can boost the selectivity and activity of SnO_2 catalyst, compared to the original SnO_2, and the carbon supports Sn.

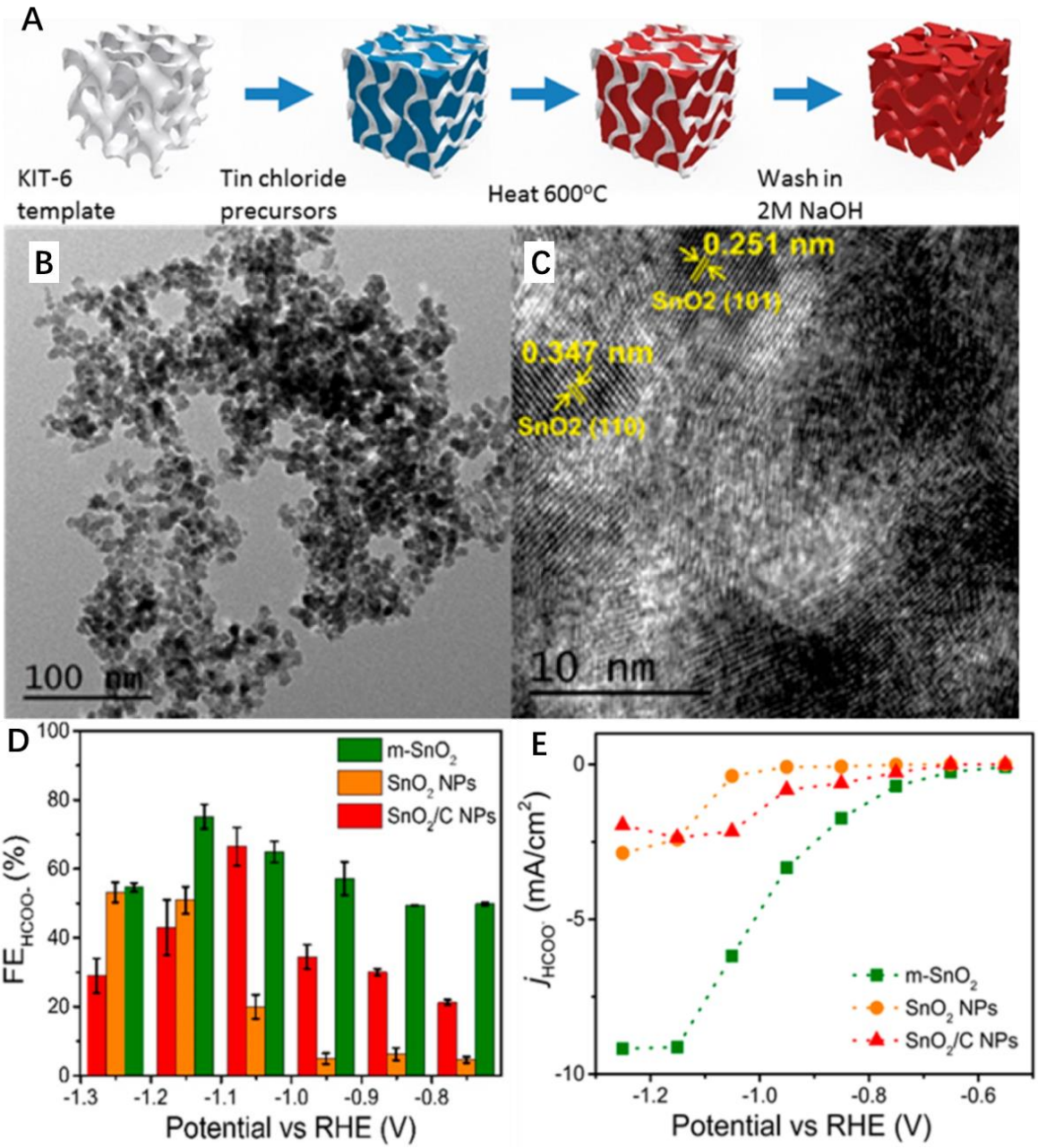

Figure 1.8 A) fabrication of m-SnO_2 catalyst B) TEM images for m-SnO_2 C) high-magnification for m-SnO_2 D) FE of $HCOO^-$ for m-SnO_2, SnO_2 NPs and SnO_2/C NPs E) partial current density for $HCOO^-$ for m-SnO_2 SnO_2 NPs and SnO_2/C NPs. Reproduced with permission.[95] Copyright 2018, American Chemical Society.

1.5 Synthesis Method for Porosity in carbon-based Materials

Several synthesis methods, such as the template-assisted method, chemical vapour deposition (CVD), thermal treatment, can construct the porous structure in carbon-based materials. The template-assisted is a classical method to obtain the porous structure. It utilizes the different soft or hard templates to form micro-, meso- and hierarchical pores in carbon-based materials. The chemical vapours deposition (CVD) method is utilized to prepare hollow carbon spheres. The precursors continuously evaporate and deposit on silica or another template. After etching the silica or another template by acid treatment, hollow carbon spheres are obtained. The thermal treatment of metal-organic frameworks (MOF) contributes to the formation of nanoporous carbon due to the evaporation of the metal and partial fusion. These methods could be used to prepare porous carbon-based materials.[96] However, some of the strategies could not be used in the synthesis of porous carbon-based catalysts.

1.6 Thesis Objective

Fe-N-C single-atom catalysts have been revealed to be comparable with the best CO-production noble metal catalysts such as Au at low overpotentials (< 500 mV), surpassing Co and Ni-based single-atom catalysts.[15,77] Also, the Fe element is more abundant on Earth with lower costs in comparison to Co. The development of single-atom Fe-N-C catalysts is thus very promising in terms of these two aspects for CO_2ER. However, the current density of Fe-N-C single-atom is relatively low at low overpotential. To avoid the formation of HER-active Fe nanoparticles, the Fe loading

is normally at a low level which negatively impacts the performance of Fe-N-C. The porous structures expose more Fe-N sites, which would enhance the performance of Fe-N-C catalysts.

This thesis aims to develop an effective method to synthesize a porous the Fe-N-C single-atom catalyst to enhance the performance of the conventional Fe-N-C single-atom catalyst. ZIF-8 was employed as the organic precursor to synthesize the Fe-N-C structure by pyrolysis in a tube furnace. The template method and amorphous SiO_2 coating on ZIF-8 were utilized to create a porous structure. In this context, the Fe-N-C catalyst with mesoporosity was synthesized successfully by an amorphous SiO_2-protected strategy, and a more profound understanding of the influence of mesoporosity for CO_2ER was gained. This thesis will provide useful insights into the development of low-cost and efficient electrocatalysts for CO_2ER.

Chapter 2 Experimental Methods

This chapter introduces the experimental details of chemical reagents, materials characterizations, electrochemical performance, as well as the detection and quantification of CO_2ER products in this study.

2.1 Materials

The materials were directly used as received without special treatment and listed in **Table 2.1** according to their applications.

Table 2.1 Materials Details

Materials	Purity/ average Mw	Company	Application
Tetraethyl orthosilicate (TEOS)	99%	Sigma-Aldrich	Synthesis of nano SiO_2
Ammonia	30%	Chem-Supply Australia	
Polyvinylpyrrolidone	29000	Sigma-Aldrich	
Ethanol	95%	Chem-Supply Australia	
Zinc acetate dihydrate	98%	Sigma-Aldrich	Synthesis of nano ZnO
Diethylene glycol (DEG)	99%	Sigma-Aldrich	
2-methylimidazole	99%	Sigma-Aldrich	Synthesis of s-Fe-N_x-C and p-Fe-N_x-C
Zinc nitrate hexahydrate	99%	Sigma-Aldrich	
CTAB	98%	Sigma-Aldrich	
Potassium hydroxide	90%	Sigma-Aldrich	
Methanol	95%	Chem-Supply Australia	

Fe(TPP)Cl	>= 94%	Sigma-Aldrich	
Nafion® 117 solution	5 wt%	Sigma-Aldrich	Gas diffusion electrode preparation
isopropyl alcohol	99%	Chem-Supply Australia	
Carbon paper (GDL 38AA)	225± 30 μm thick	SGL Carbon	

2.2 Materials Characterizations Technique

Material characterizations are significant for comprehending the catalysts and electrodes. The structure analysis and electrochemical analysis would reveal the relationship between the mesoporous structure and the electrocatalytic performance, facilitating the rational design of the electrocatalyst for CO_2ER. Here, the physical characterizations and electrochemical measurements in this thesis are introduced in detail.

2.2.1 Physical Characterizations

Scanning electron microscopy (SEM) was used to obtain the micro-morphology of the catalysts. Transmission electron microscopy (TEM) and scanning transmission electron microscope (STEM) were also carried out to obtain the highly magnified image. High-angle annular-dark-field (HAADF-STEM) and energy-dispersive X-ray spectroscopy (EDS) were employed to detect single atom confinement and elemental contribution, respectively. The X-ray diffraction (XRD), X-ray photoelectron spectroscopy (XPS), and Raman spectroscopy were used to investigate the catalyst surface, composition, and structure information.

2.2.1.1 Scanning Electron Microscopy

SEM is a fundamental microscopy technique that can be used to investigate the morphology of the catalysts.[97] The principle of the SEM is that a high-energy beam of electrons was used to scan the surface of the samples. And the scan electrons directly strike with atoms of the specimen, generating a variety of signals that form the image of the catalyst surface and composition. In most situations, the SEM model collects the secondary electrons, which is excited by the high-energy electron beams. However, the SEM image cannot provide enough information due to the low magnified image.

In this work, ZIF-8 was coated 10 nm Pt under plasma sputtering as it is not electrically conductive. After thermal treatment, the Fe-N-C single-atom catalysts were electrically conductive. In this work, all the samples are directly attached to an aluminum sample holder using carbon tape and put in the vacuum chamber for SEM observation. All the SEM images were collected in NanoSEM 450.

2.2.1.2 TEM, STEM, HAADF-STEM, EDS

TEM was utilized to obtain the highly magnified image of the sample to a deeper understanding of the morphology.[98] The principle of TEM is that a beam of electrons transmits across a thin specimen (less than 100 nm thickness) to generate a highly magnified image. STEM is an important model in TEM system for single-atom catalysts because it provides an atomic resolution image. Under the STEM model, the electron beam is focused into a spot on the specimen and gradually scan each atom row, finally simulating into an atomic-level resolution image. The energy-dispersive X-ray

spectroscopy (EDS) detector attached on the TEM can also identify the elemental contribution on the samples. The high-angle annular-dark-field (HAADF), reflecting the Z number of the particular element, can also be collected at the same time to cross-confirm the existence of single atom status under different shades. The aberration-corrected STEM can clearly identify the single atomic columns in the catalysts, which prove the single atom status. The aberration corrector is incorporated in the probe-forming lens system and provides a nominal beam diameter of 0.07 nm at an aperture semi-angle of 26.5 mrad and probe current of 23 pA.[99]

Particularly, the Philips CM200 field emission transmission electron microscope was used to collect the HR-TEM images. The atomic resolution images were observed by JEOL JEM-ARM200F. The samples were well-dispersed in ethanol, and 15 μL diluted suspension was dropped on copper gird.

2.2.1.3 X-ray Photoelectron Spectroscopy

XPS is an outstanding technique for investigating the surface composition and the electronic state.[100] the detector records the kinetic energy of the photoelectron and The number of electrons that escape from samples. Normally, the XPS analyses the depth of the 10 nm for materials.

A Thermo ESCALAB250Xi X-ray photoelectron spectrometer was used to obtain the XPS spectra with Al Kα (1486.6 eV). The specimen powders were attached to the Al holder by carbon conductive tape and immediately tested without special treatment.

2.2.2 Electrochemical Characterization

To estimate the properties of the electrocatalysts to CO_2ER, linear sweep voltammetry (LSV) and constant potentials amperometry (CPA) were generally used to the electrochemical performance.

2.2.2.1 LSV

LSV is an electrochemical technique to evaluate the performance of the catalyst. LSV can reveal the relationship between the total currents and applied potentials, which can be used to a general estimate of the catalytic activity. LSV also indicates the onset potential. The principle of the LSV is that the responding current at the working electrode is measured while a linearly changing voltage is applied between the working electrode and the reference electrode. (As shown in **Figure 2.1**)

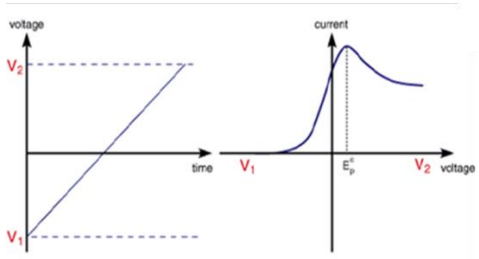

Figure 2.1 Applied linearly changing voltage and corresponding varying current.

2.2.2.2 CPA

CPA is an essential technique to estimate the catalyst's performance of CO_2ER. The principle of CPA is that constant voltages were applied between work and reference electrodes while the corresponding current was recorded. According to the CPA results, the faraday efficiency and current density can be calculated. It is also used to evaluate

the stability of the catalysts. These parameters are significant to estimate the CO_2ER performance of the electrocatalysts.

2.2.2.3 Experiment Measurements

In this thesis, the electrochemical measurements were carried out on the Electrochemical (Workstation CHI760D) with a standard H-cell with three-electrode system. The Pt plate was used as the counter electrode. The saturated calomel electrode (SCE) was used as the reference electrode. In the chapter 3, the fabrication of the working electrode is as the following procedure:12 mg of catalyst and 30 μl 5% Nafion solution were introduced into 970 μl of ethanol solution and sonicated for 30 mins; 60 μl catalyst ink was dropped onto a 1cm × 1cm commercial gas-diffusion layer (GDL) attached carbon paper substrate and dried in the air, giving a catalyst loading of 0.72 mg cm^{-2}. 0.5M CO_2-saturated $KHCO_3$ was used as the electrolyte. Electrochemical data was corrected with 90% IR compensation. According to the Nernst equation, all potentials were calculated with respect to the reversible hydrogen electrode (RHE) as the following equation ($E_{RHE} = E_{SCE} + 0.0591 \times pH + 0.241$ V, at 25 °C).

2.3 Identification of CO_2 Product

Products detection and analysis are the key factors to investigate the performance of the CO_2 reduction. Various gas products may be generated during the electrolysis at different potentials. The gas chromatography (GC) technique was used to analyze and quantify the aimed gas-product of CO_2ER in this project.

2.3.1 Gaseous Products Analysis

In this thesis, as shown in **Figure 2.2**, gas chromatography (SRI 8610C 3#), flowmeters were employed to establish for the on-line gas analysis system. A moisture trap and a hydrocarbon trap were used to purify the H_2 carrier gas for the flame ionization detector (FID). While a moisture trap and an oxygen trap purify the Ar carrier gas for the thermal conductivity detector (TCD). Therefore, the sensitivity of the two detectors is enhanced by gas purification systems. The flow rate of Ar and CO_2 depends on the low-pressure needle valve and a mass flower, respectively. The gas flow rate at the outlet of the GC was calibrated by a bubble flowmeter. The low-temperature chiller was employed to remove the moisture in the gas mixture and vented to the GC, which minimizes the negative influence on the molecular sieve column.

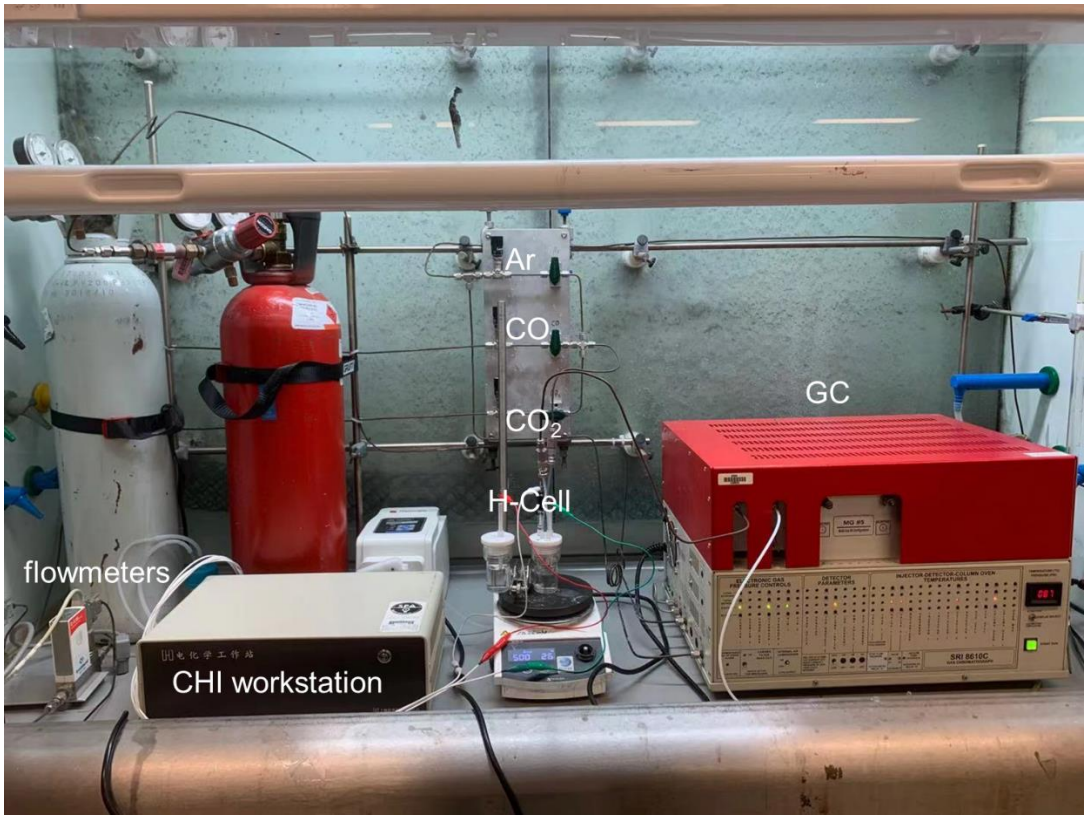

Figure 2.2 The image of on-line analysis system for CO_2ER.

The SRI GC contains a packed MolSieve 5A column and a pack Haysep D column. With the carrier gas of argon, the concentrations of target CO and/or hydrocarbons (CH_4, C_2H_4 and C_2H_6) can be detected and quantified by the FID, while the TCD is associated to measure the H_2 product. The FID detector was able to detect hydrocarbons at concentrations 1 ppm level. The type of calibration curves for the hydrogen, carbon monoxide, methane, ethylene, and ethane are shown in **Figure 2.3.**

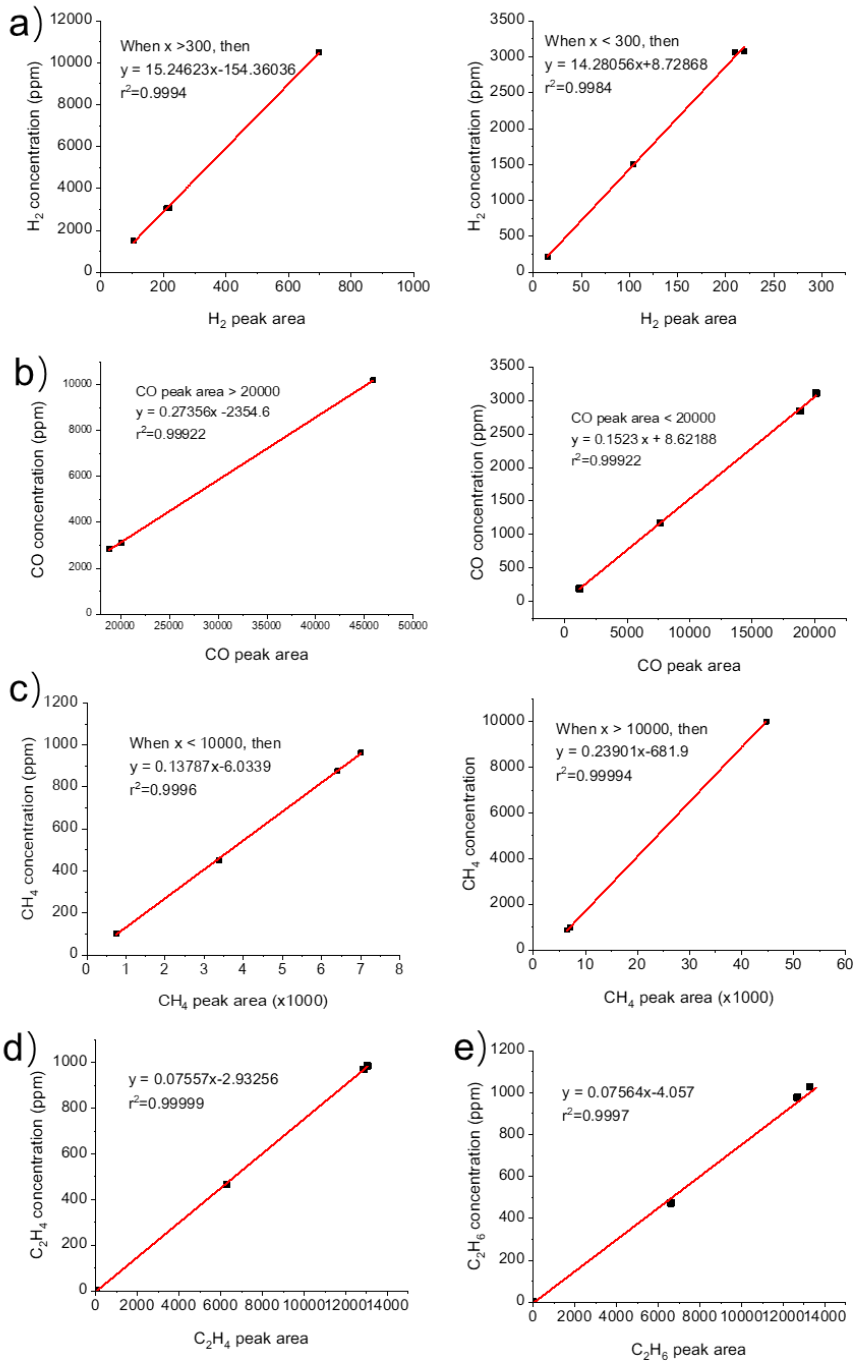

Figure 2.3 Peak areas and the corresponding concentration curves for GC, a) H_2, b) CO, c), CH_4, d) C_2H_4, e) C_2H_6.

The experiments were performed in a gas-tight H-cell with two compartments separated by a proton exchange membrane (PEM, Nafion®117), shown in **Figure 2.4**. The Nafion membrane was used to prevent the reduction products from being

oxidized on the anode. 30 mL electrolyte (0.5 M $KHCO_3$) was added into each compartment. To avoid the negative influence of O_2 in the electrolyte, the electrolyte in the work compartment was purged by the CO_2 (99.99%) for 30 mins. To improve the mass transfer of CO_2 to the working electrodes, a 1 cm magnetic stirring bar stirred the electrolyte at 500 rpm. In the whole electrolysis process, the flow rate of the CO_2 in the work compartment was 20.0 mL/min, which was controlled by a flowmeter. The flow-rate was calibrated with a manual soap-film flowmeter at the outlet of the GC. 1 mL gas sample in a gas-sampling loop was injected into the system by rotating a six-way valve, and then GC started to run was for 20 min (14 min for GC running and 6 min for cooling down). An average of three or four measurements was used in data analysis.

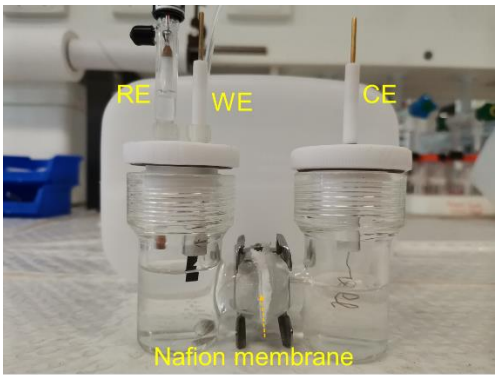

Figure 2.4 Photo of the standard three-electrode system in PEM H-Cell

Chapter 3 Atomically dispersed Fe-N_x sites on Mesoporous Carbon with Enhance Mass Transport for Selective CO_2 Electroreduction.

3.1 Introduction

Atomically dispersed metal (e.g. Fe, Ni, Co, Mn) anchored nitrogen-doped carbons substrates (M-N-C) have exhibited excellent electrocatalytic performance of CO_2 conversion to CO.[85, 89, 101] The metal-nitrogen moieties (M-N_x) are considered as active sites in M-N-C catalysts. The performance of these active sites is highly affected by the local chemical environment around the central metal sites.[102-105] Increasing the metal loading in the structure is an effective method to enhance the performance. However, the synthesis of M-N-C catalyst via thermal treatment pyrolysis method inevitably suffer from partial fusion and aggregation, which contribute to the formation of mixed the M-N_x species and metallic aggregates on M-N-C catalysts.[73, 75, 106, 107] As a result, the density of M-N_x sites is reduced, and the CO_2ER performance is deteriorated due to the presence of HER-active metal clusters or nanoparticles. To avoid the generation of these transition metal nanoparticles, the metal loading in M-N-C materials is generally at a low level.[75, 108]

To further enhance the performance of this kind of catalyst, it is favourable to build a hierarchical porous structure for anchoring the atomically dispersed metal atoms. Compared with the conventional M-N-C catalysts, the M-N-C catalysts with hierarchical porous structures has two advantages. First, the mesoporosity improves the

specific surface area, thus achieving more exposed of M-N_x active sites. Second, the morphology and porosity of catalysts can facilitate the mass transfer and CO_2ER kinetics.[92, 93] Hence, the catalytic activity and product selectivity of the CO_2ER can be further enhanced.[79] At present, most studies of porous M-N-C catalysts have only investigated the influence of a large specific surface.[79 95] However, the role of porous structures in the mass transfer is still unclear.

To investigate the effect of porous structure for mass transfer in CO_2ER, zeolitic imidazolate framework-8 (ZIF-8) was prepared as precursors to synthesize highly porous carbon nanoparticles. Additionally, various templates and amorphous SiO_2 coating were investigated to obtain mesoporous structures on carbon nanoparticles. The synthetic process involves the ZIF-8 amorphous SiO_2 coating and thermal treatment. The morphology of the carbon nanoparticles is controlled by the thickness of the SiO_2 shell. After forming the porous structure, the porous carbon absorbs the 5,10,15,20-tetraphenyl-21H,23H-porphine iron (III) chloride (Fe-TPP) molecular, followed by 600 ℃ thermal treatment. Finally, the Fe-N_x-C catalysts with the hierarchical porous structure were obtained. Compared with the Fe-N_x-C, the obtained Fe-N_x-C catalysts with the hierarchical porous exhibit excellent activity toward the CO_2 conversion CO.

3.2 Experiment Section

3.2.1 Materials

Zinc nitrate hexahydrate ($Zn(NO_3)_2 \cdot 6H_2O$ 99%), 2-methylimidazole (99%), methanol (95%), ethanol absolute (95%), potassium hydroxide (KOH, 90%), Zinc

acetate dihydrate (98%) diethylene glycol (DEG, 99%) cetyltrimethylammonium bromide (98%), tetraethyl orthosilicate solution (99%), Potassium bicarbonate (99.95%), 5,10,15,20-tetraphenyl-21H,23H-porphine iron(III) chloride (>= 94%). All reagents and solvents were used as received. Carbon paper (Sigracet GDL 38AA, 225±30 μm) purchase from SGL Carbon GmbH. Nafion membrane (117) was from Alfa-Aesar. The water used was ultrapure Milli-Q water (18.2 MΩ cm).

3.2.2 Catalyst preparation

3.2.2.1 Synthesis of Nano-SiO_2@ZIF-8 Core-shell Material

The nano-SiO_2 sphere was used as the template. It was synthesized by adopting a Stöber method.[109] Typically, 4.5 ml of TEOS was added into 45.5ml ethanol solution, followed by adding the mixture 16.3 ml of ethanol, 9.0 ml of ammonia and 24.8 ml of water. Then, the mixed solution was stirred for 1 hour at room temperature. Finally, the nano-SiO_2 sphere was collected by centrifuging and washing three times with water and dried at vacuum at 60 ℃ overnight. The 100 mg of the as-prepared nano-SiO_2 was added into 200 mL methanol solution containing 1.695g Zinc nitrate hexahydrate, 1.97g 2-methylimidazole and 100 mg PVP. After that, the mixture was stirred at room temperature for 24 hours. Nano-SiO_2@ZIF-8 core-shell material was collected by centrifuging and washing three times by methanol.

3.2.2.2 Synthesis of Nano-ZnO@ZIF-8 Core-shell Materials

The nano-ZnO sphere was prepared by a previously reported method.[110, 111] 5.49 g

zinc acetate dihydrate dissolved into 250 ml DEG, and the mixture was heated at 160 ℃ for 1 hour under reflux conditions. After cooling down to room temperature, the product was centrifugated and washed 3 times by ethanol and dried in a vacuum at 60 ℃.

The were nano-ZnO@ZIF-8 core-shell synthesized by a report work.[112] 100 mg of nano-ZnO was added into10 mL methanol solution and sonicated for 30 mins, which was subsequently added into 27 mL 2-methylimidazole methanol solution (3.66 mol/L). Then the ZIF-8 was grown on the surface of nano-ZnO by stirring 1 hour at room temperature. The nano-ZnO@ZIF-8 core-shell was collected by centrifuging and washing 3 times by ethanol and dried in a vacuum at 60 ℃.

3.2.2.3 Synthesis of Zeolitic Imidazolate Framework-8 (ZIF-8)

ZIF-8 was synthesized by a modified reported method.[101, 108] 3.39g $Zn(NO_3)_2 \cdot 6H_2O$ was added into 180 mL methanol, followed by adding 180 mL methanol solution containing 3.94g 2-methylimidazole (MeIM). The ZIF-8 was obtained by stirring for 24 h at 60 ℃ temperature. The ZIF-8 powder was collected by centrifuging, washing with methanol three times, and dried overnight in a vacuum oven at 60 ℃ overnight.

3.2.2.4 Synthesis of SiO_2 Coated ZIF-8 Nanoparticles (SiO_2@ZIF-8)

SiO_2 coated ZIF-8 was prepared by modified with report method.[79] The prepared ZIF-8 (300 mg) was dissolved in 120mL of water, followed by adding 3 mL of aqueous cetyltrimethylammonium bromide (CTAB) solution (25mg mL^{-1}) and 5 mL of aqueous KOH solution (6mg mL^{-1}). Tetraethyl orthosilicate (600 μL) was dissolved in 3 mL of

methanol and then added into the above solution under stirring for 0.5 h. The precipitated solid (SiO_2 @ ZIF-8) was collected by centrifuging, washing three times with ethanol, and dried at 60 °C overnight.

3.2.2.5 Synthesis of Fe-N_x-C with Porosity (p-Fe-N_x-C)

The obtained SiO_2 @ ZIF-8 powder was put into a tube furnace and heated to 1000℃ for 3 hours in the N_2 atmosphere with 5 ℃/min. Then SiO_2 coated N-C powder was obtained and further added into 25mL KOH aqueous solution (2 mol/L) and stirred 24 hours at 80 ℃ to remove the SiO_2 shell. Then, the porous carbon was centrifuged and washed with methanol four times and dried in a vacuum oven at 60 ºC overnight. Then 60 mg N doped porous carbon was dispersed into 20 mL ethanol containing 13.4mg Fe-TPP molecules and sonicated for 30 mins. After that, the solution was heated to 80 ℃ for 12 hours to volatilize the ethanol solution. When the solution is dried out, the black powders are placed into the tube furnace and heat 600℃ for 2 hours in N_2 atmospheres.

3.2.2.6 Synthesis of Fe-N_x-C without Porosity (s-Fe-N_x-C)

The prepared ZIF-8 (300 mg) was placed into the tube furnace and heated to 1000℃ for 3 hours in the N_2 atmosphere. After that, the 60 mg N doped carbon was added into 20 mL ethanol containing 13.4 mg Fe-TPP molecules and sonicated for 30 mins. Then the solution was heated to 80 ℃ for 12 hours to volatilize the ethanol solution. When the solution dries out, the black powders are put into the tube furnace and heat 600 ℃ for two hours in N_2 atmospheres.

3.3 Results and Discussion

Using a hard template is a comment method to synthesize nanomaterials with porous structures. The nano-SiO_2 and nano-ZnO was investigated as the template. As shown in **Figure 3.1** a, the size of nano-SiO_2 is 400 to 500 nm. The ZIF-8 could not cover the surface of the nano-SiO_2 completely. Hence the template methods are not suitable for the synthesis of the carbon nanoparticles with mesoporosity. The SEM of nano-ZnO (**Figure 3.1** b) indicates that the size of the nano-ZnO sphere is 200 to 300 nm which is accordant with the report. The SEM of Nano-ZnO@ZIF-8 Core-shell materials was displayed in **Figure 3.1** c. It is clear that the ZIF-8 coat Materials the surface of nano-ZnO thoroughly. Finally, the nano-ZnO@ZIF-8 core-shell materials was pyrolyzed at 600 ℃ in the N_2 atmosphere for 2 hours. Then, the N carbon cover nano-ZnO was heated at 800 ℃ in the N_2 atmosphere for 1 hour. Finally, the sample was put into 50ml 3M HCl for ZnO template removal. The image of the sample reveals that the N doped carbon without porous structure **(Figure 3.1** d). Hence, we change the synthetic strategies.

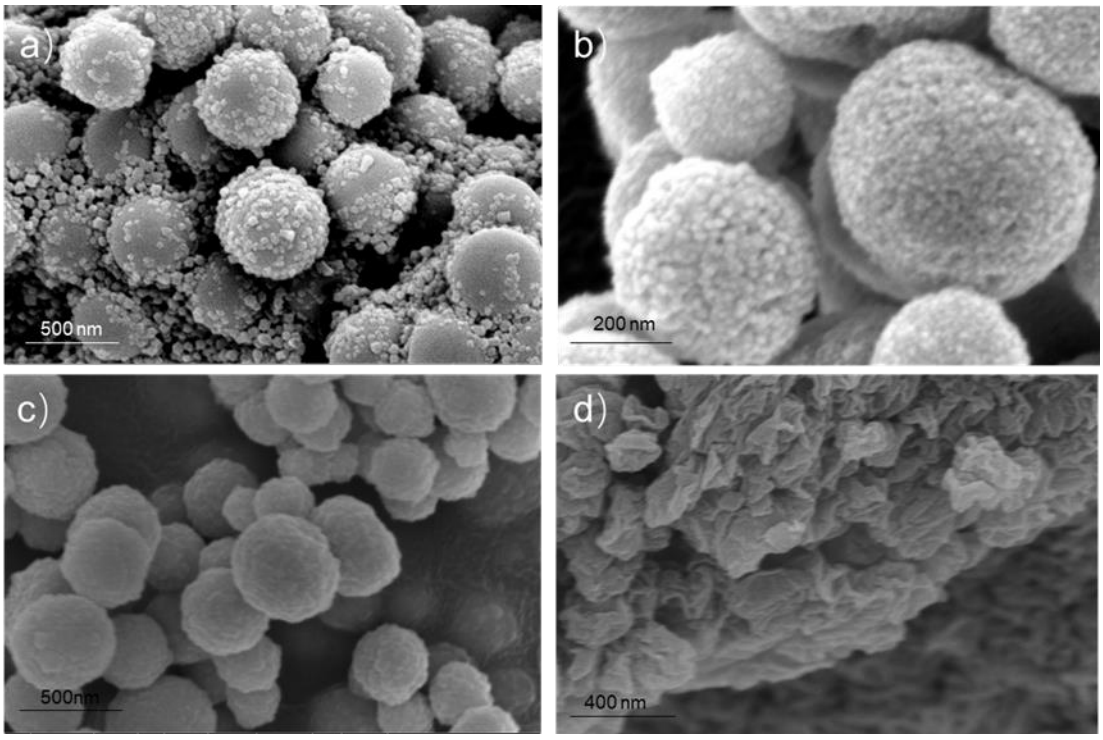

Figure 3.1 a) SEM image for the Nano-SiO_2@ZIF-8 core-shell. b) SEM image for the nano-ZnO sphere. c) SEM image for nano-ZnO@ZIF-8 core-shell. d) SEM image for N-doped carbon with the template removal.

The silica-protected strategy was used to synthesise the porous Fe-N_x-C catalyst, which was schematically described in **Figure 3.2** a.[113] The ZIF-8 was fabricated by a reported method that the zinc nitrate and 2-methylimidazole were mixed in the methanol solution. The ZIF-8 precipitates were centrifuged and washed by methanol. Next, the ZIF-8 nanoparticles were covered by a layer of amorphous SiO_2 through alkali catalyzed hydrolysis of tetraethyl orthosilicate in the presence of cetyltrimethylammonium bromide. Then, pyrolysis of SiO_2 @ ZIF-8 1000 ℃ results in the formation N doped carbon due to the volatilization of the Zn node (b.p. = 907 ℃). During the high-temperature treatment, normally ZIF-8 crystal would be shrunk due to the mass loss. However, the ZIF-8 could maintain due to an external SiO_2 coating layer

while the planar faces collapsed, contributing to the formation of the mesoporosity.[114] The N-doped carbon nanoparticles with the porous structure were obtained by etching the SiO_2 shell in a KOH aqueous solution. Finally, the N-doped carbon porous adsorption of the Fe-TPP molecules and Fe and N co-doped porous carbon (p-Fe-N_x-C) nanoparticles was formed after a thermal treatment.

As revealed by SEM (**Figure 3.2** c), the p-Fe-N_x-C nanoparticles are uniform in size of 60-70 nm, and different from the initial ZIF-8 shape. Additionally, the HAADF-STEM provides more details of the catalyst. The average diameter of mesopores is 5 nm to 20 nm. No Fe nanoparticle was observed in the structure (**Figure 3.2** b). Many homogeneously distributed bright spots were observed on the carbon surface in aberration-corrected HAADF-STEM image (**Figure 3.2** f), which is ascribed to the single Fe atoms due to the different Z contrasts of Fe, N and C elements. The elemental distribution for N and Fe is described by the energy-dispersive spectroscopy mapping (**Figure 3.2** g), which demonstrates that Fe and N are homogeneously dispersed on the surface of the carbon matrix.

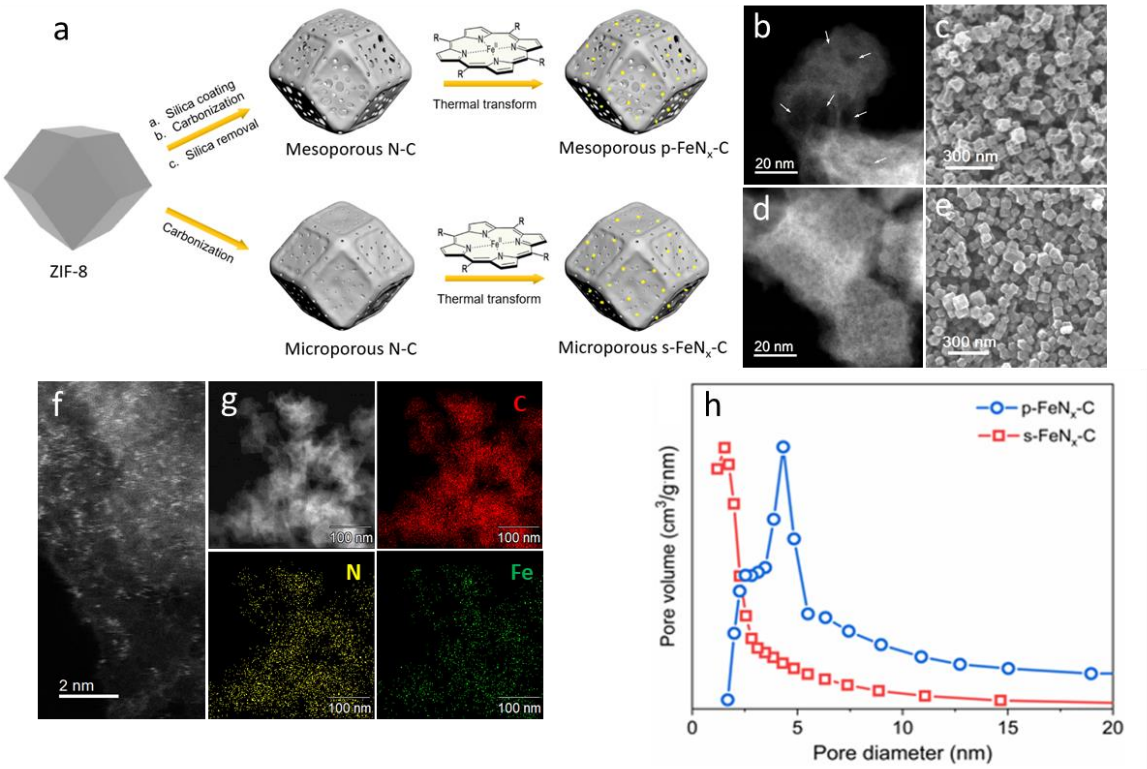

Figure 3.2 a) Scheme illustration for synthesis pathway for p-Fe-N_x-C and s-Fe-N_x-C. b) HAAF-STEM image of p-Fe-N_x-C, c) SEM image of p-Fe-N_x-C. d) HAADF-STEM image of s-Fe-N_x-C, e) SEM image for s-Fe-N_x-C. f) High-resolution HAAF-STEM image for p-Fe-N_x-C. g) EDS mapping for p-Fe-N_x-C. h) pore size distribution for p-Fe-N_x-C and s-Fe-N_x-C.

The synthetic route for control sample s-Fe-N_x-C was also described in **Figure 3.2** a**.** In simple terms, the obtained ZIF-8 was directly carbonized into N-doped carbon at the1000 ℃ in N_2 atmosphere. Then the N doped carbon absorbed the Fe-TPP molecules to form the s-Fe-N_x-C catalyst. The SEM image (**Figure 3.2** e) reveals that after high-temperature treatment and adsorption of Fe-TPP molecules, s-Fe-N_x-C nanoparticles maintain the origin rhombic dodecahedron shape with distinct edges. The HAADF-STEM image (**Figure 3.2** d) indicates that s-Fe-N_x-C nanoparticles are uniform in size

(70-80nm), and no Fe particle is formed. The isolate Fe atoms were observed in the Aberration-Corrected high-resolution HAADF-STEM image (**Figure 3.3** a). The EDS mapping demonstrates the uniform distribution of N and Fe atoms on the surface of s-Fe-N_x-C (**Figure 3.3** b).

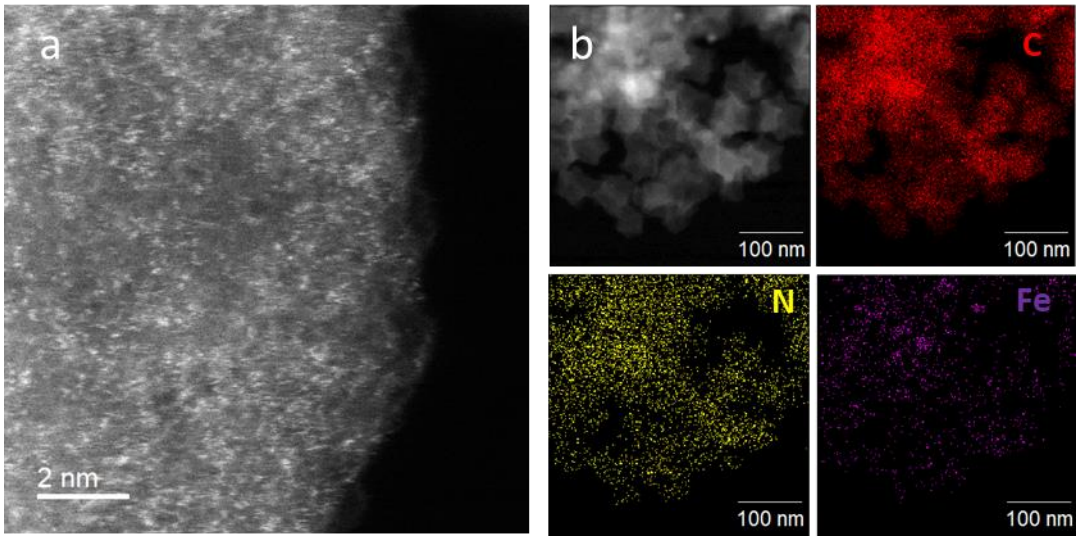

Figure 3.3 a) aberration-corrected HAADF-STEM image for s-Fe-N_x-C. b) EDS spectrum for s-Fe-N_x-C.

The BET measurements were utilized to investigate the pore distribution and the specific surface area of p-Fe-N_x-C and s-Fe-N_x-C. As shown in **Figure 3.2** h, s-Fe-N_x-C demonstrated one distinct micropore with a diameter of 2 nm, which were generated by the evaporation of Zn species during the high-temperature process.[74, 115, 116] Compared with the s-Fe-N_x-C, the p-Fe-N_x-C had a mesopore with diameters of 5 nm, which was corresponding with the HAADF-STEM results. The BET surface area of p-Fe-N_x-C is 526.09 m^2/g. However, the BET surface area of s-Fe-N_x-C (901.5 m^2/g) is larger than p-Fe-N_x-C. (**Table 3.1**) These results are different from others studies.[79, 114] The reason may be that after etch by aqueous KOH solution, some SiO_2 particles not be removed completely, which could occupy the micropores in the p-Fe-N_x-C structure.

Table 3.1 BET results of catalysts.

Sample name	BET area (m^2/g)	Pore volume (cm^3/g)	Average pore size (nm)
s-N-C	1499.21	1.10	3.30
s-Fe-N_x-C	901.51	0.70	3.29
p-N-C	1139.41	1.60	6.99
p-Fe-N_x-C	526.09	1.03	9.30
FeTPP/p-N-C	376.03	0.96	10.84

XPS was employed to characterize the catalyst surface and composition (**Figure 3.4** a). The high-resolution N 1s spectra of both samples indicate the presence of pyridinic-N (398.4 eV), pyrrolic-N (400.0 eV), graphitic-N (401.2 eV), and N-oxide (403.2 eV), respectively. Fe 2p3/2 spectrum reveals that the Fe atoms were oxidized from +2 to +3, indicating the atomically dispersed Fe atoms on the carbon matrix without Fe nanoparticles (**Figure 3.4** b). This result was also proved by the X-ray diffraction patterns (**Figure 3.4** c), where no diffraction peaks related to Fe aggregation was observed in both catalysts. Two broad and weak diffraction peaks at around 25° and 44° correspond to (002) and (100) planes of graphitic carbon, respectively, indicating both samples are highly amorphous. The Raman spectra were used to analyse carbon structures of the p-Fe-N_x-C and s-Fe-N_x-C. As displayed in **Figure 3.4** d, two main peaks were observed at 1352 and 1580 cm^{-1} corresponding to D-band and G-band, respectively, indicating disordered carbon and graphitic sp^2 carbon in both catalysts. The D-band to G-band ratios of the two catalysts are almost similar (1.04),

demonstrating a similar defective degree of both carbon substrates. Inductively coupled plasma optical emission spectrometry results (**Table 3.2**) exhibit the similar Fe content of both catalysts, in which p-Fe-N_x-C is 1.27% and s-Fe-N_x-C/ is 1.38%. ICP-OES results also indicate p-Fe-N_x-C and s-Fe-N_x-C contain Zn elements, which correspond with the previous report.[77] Normally, Zn-N-C can convert the CO_2 into CH_4.[117] However, the GC results here reveal H_2 and CO are the only two products. Therefore, Zn sites in catalysts do not contribute any catalytic activity on CO_2ER.

Table 3.2 ICP-OES-results for the p-Fe-N_x-C and s-Fe-N_x-C

Sample name	**Fe (w%)**	**Zn(w%)**
s-Fe-N_x-C	**1.38**	**4.37**
p-Fe-N_x-c	**1.27**	**3.08**

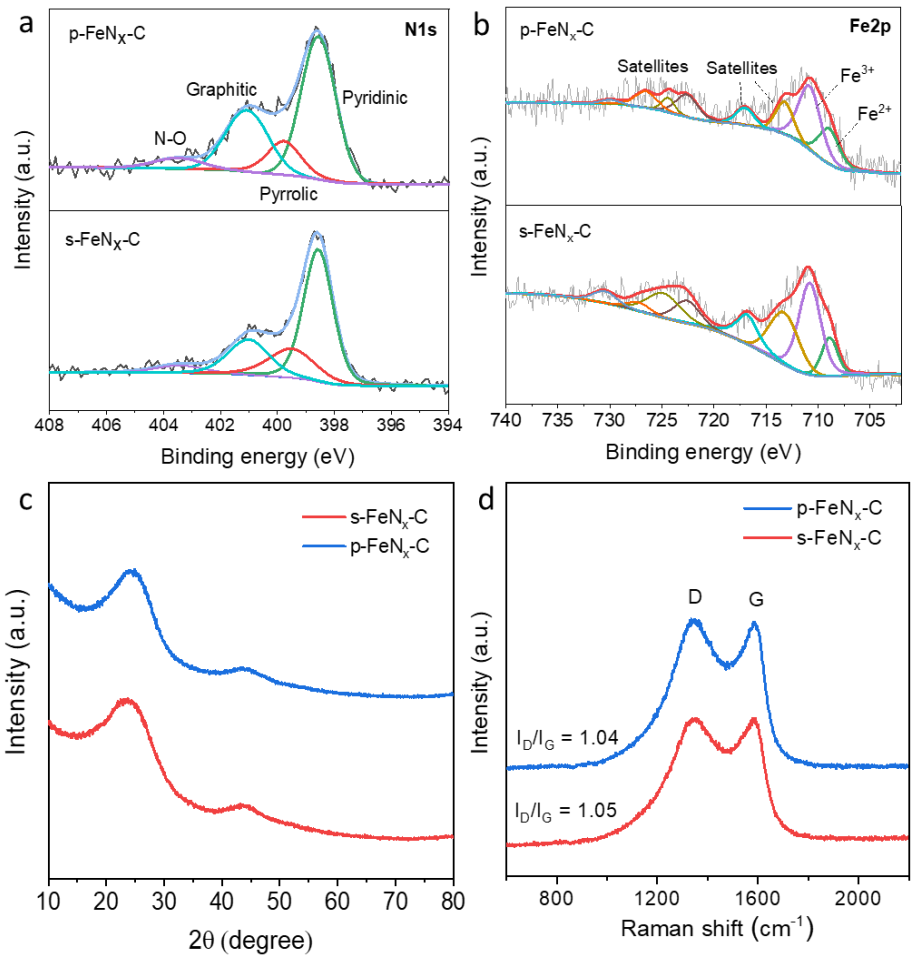

Figure 3.4 a) High-resolution XPS N 1s spectra, b) High-resolution Fe 2p, c) XRD patterns, d) Raman spectra of s-Fe-N_x-C and p-Fe-N_x-C.

The electrocatalytic performance of p-Fe-N_x-C, s-Fe-N_x-C for CO_2ER was measured in a three-electrode H-cell system with the CO_2-saturated 0.5M $KHCO_3$ aqueous electrolytes. From the line sweep voltammetry (LSV) results in **Figure 3.5** a, s-Fe-N_x-C and p-Fe-N_x-C demonstrate the catalytic activity to CO_2ER. The total current density of p-Fe-N_x-C is higher than s-Fe-N_x-C from -0.4 V to -1.0 V, indicating a higher performance can be achieved on the porous structure. The constant potentials amperometry was utilized to investigate the detailed performance of both catalysts. On-

line gas chromatography (GC) and NMR measurements were performed to detect the gas and liquid products, respectively. The results of the GC and NMR indicate that H_2 and CO are the only two products during the reaction at all applied potentials. **Figure 3.5** b presents the Faradaic efficiency (FE) of CO for the p-Fe-N_x-C and s-Fe-N_x-C. Both catalysts reveal similar CO at -0.4 V and -0.5 V, reaching a maximum FE(CO) of 100%. With higher applied overpotentials, the FE(CO) for both catalysts present the same downward trend due to the low intrinsic activity of isolated Fe atoms at high potential. The CO partial current densities for p-Fe-N_x-C are higher than s-Fe-N_x-C at the whole potential window., demonstrating the significantly increased CO_2ER performance on the porous structure. The p-Fe-N_x-C can reach a maximum of 10.58 mA cm^{-2} at -0.7V, approximately two times higher than the s-Fe-N_x-C (**Figure 3.5** c). The calculation of the turnover frequency (TOF) further discloses the intrinsic activity of the catalyst based on the number of metal atoms involved in the reaction. The TOFs of both samples were calculated from -0.4V to -0.9V (as shown in **Figure 3.5** f). The s-Fe-N_x-C/ and p-Fe-N_x-C reach their maximum TOF of 532.4 h^{-1} and 1206.5 h^{-1} at -0.7V, respectively.

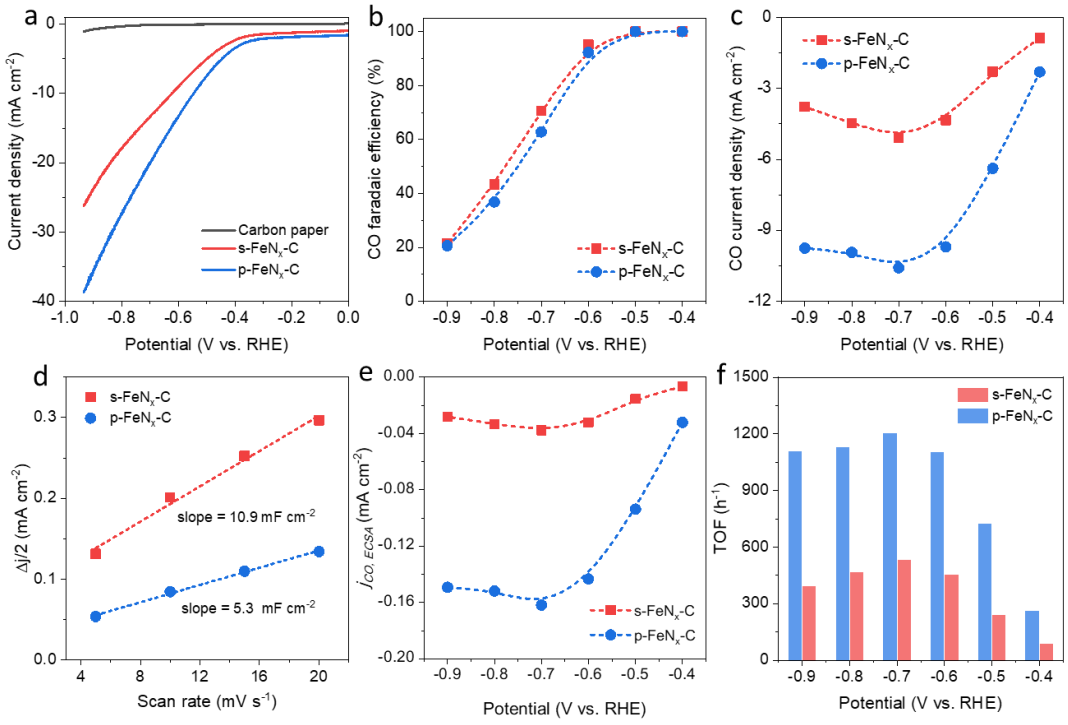

Figure 3.5 a) LSV curves of the carbon paper, s-Fe-N_x-C and p-Fe-N_x-C. b) Faradaic efficiency for CO, c) j_{co} of s-Fe-N_x-C and p-Fe-N_x-C. d) ECSA of s-Fe-N_x-C and p-Fe-N_x-C e) ECSA-normalized j_{co} of s-Fe-N_x-C and p-Fe-N_x-C. f) TOFs of s-Fe-N_x-C and p-Fe-N_x-C

To reveal the intrinsic electrocatalytic activity of CO_2ER, the CO partial current densities of CO p-Fe-N_x-C and s-Fe-N_x-C were normalized by electrochemical active surface area (ECSA). ECSA was evaluated by the double-layer capacitance (DLC) method. The DLC of examples was collected in the polished glassy carbon disk whose capacitance was 0.081 mF cm^{-2}. According to **Figure 3.5** d, the s-Fe-N_x-C reveals a larger electrochemical active surface area with 134.6 cm^2 which is about two times larger than p-Fe-N_x-C (65.4 cm^2). The ECSA-normalized CO current density for p-Fe-N_x-C is about four times higher than that of s-Fe-N_x-C at -0.7 V (**Figure 3.5** e), indicating the higher activity of Fe atoms in p-Fe-N_x-C than s-Fe-N_x-C. Therefore, the

above results clearly demonstrate the advantages of the porous structure that can significantly increase the CO_2ER performance.

To deeply understand the role of the mesopores in CO_2ER, electrochemical impedance spectroscopy (EIS) was performed on two catalysts. The impedance arc of p-Fe-N_x-C is remarkably smaller than that s-Fe-N_x-C at low frequency, where the arc diameter implies the diffusion behaviour of reactants (**Figure 3.6** a). This indicates that the p-Fe-N_x-C possesses a much smaller diffusion resistance for the reactant CO_2 gas at the interface during the CO_2ER in comparison to the control s-Fe-N_x-C. To investigate the influence of the mesoporous structure on the CO_2 transfer, the electrocatalytic performance of p-Fe-N_x-C and s-Fe-N_x-C were further tested at the different CO_2 partial pressures (P_{CO2}). According to Anna's study,[118] the relationship between the j_{CO} and P_{CO2} reveals the CO_2 transfer capacity of the catalyst, which further affect the activity. Therefore, relevant experiments were designed to expose this relationship in the Fe-N-C catalysts. Different CO_2 concentrations (40% to 100%) were obtained by introducing different contents of Ar gas. The performance of p-Fe-N_x-C and s-Fe-N_x-C/s were tested at -0.5V with diluted CO_2. The results reveal that the CO FEs of both catalysts decrease with the decline of CO_2 concentrations (**Figure 3.6** b). The relationship between the j_{CO} and P_{CO2} was described in **Figure 3.6** c. With the concentration of CO_2, the increase of j_{CO} for p-Fe-N_x-C was higher than s-Fe-N_x-C. The slope of the p-Fe-N_x-C is 0.054, while that of s-Fe-N_x-C is 0.029. These results indicate the porous Fe-N-C single-atom catalyst (p-FeN_x-C) is more significantly affected by the decreasing CO_2 transport at the reaction interface than the catalyst without abundant

mesopores (s-Fe-N_x-C). This difference demonstrates the benefits of mesopores in CO_2 gas transport again.

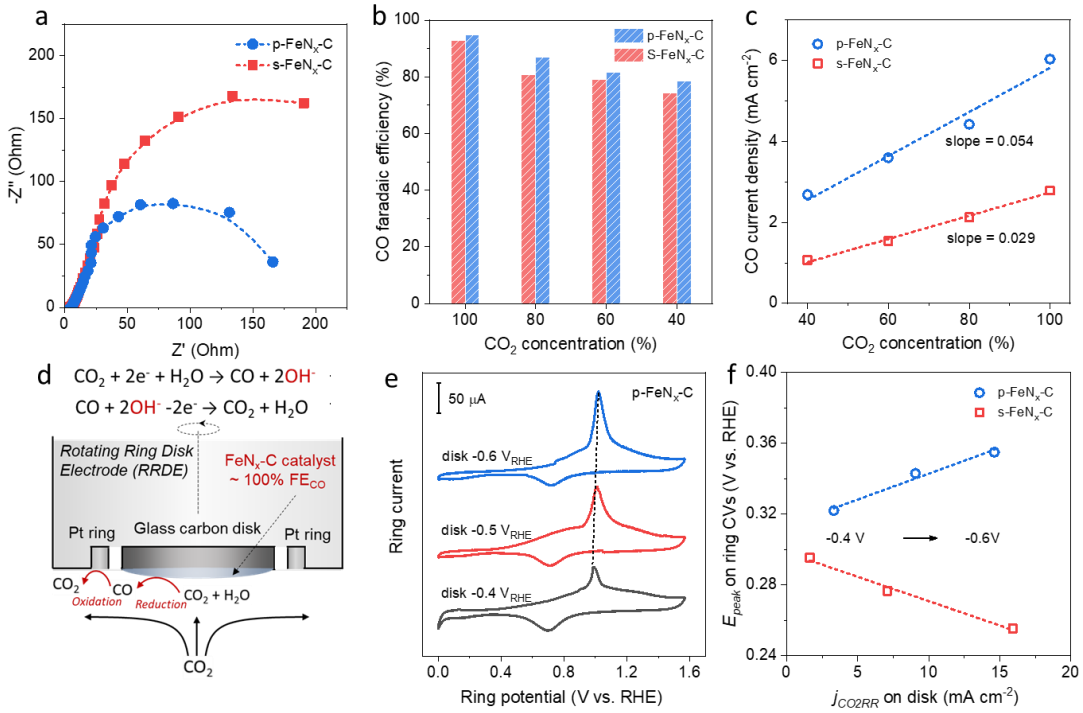

Figure 3.6 a) Nquist plots tested in CO_2-saturated 0.5M $KHCO_3$ aqueous solutions at 0V vs. RHE, b) CO Faradaic efficiencies on the different P_{CO2} at -0.5V vs. RHE, c) P_{CO2} dependence of the CO partial current densities at-0.5V vs RHE for p-Fe-N_x-C, s-Fe-N_x-C, d) Scheme illustration for RRDE, e) Cyclic voltammograms (CVs) of CO oxidation collected by the Pt ring electrode, f) Observed peak potential E_{peak}.

Besides, studies have indicated that local pH near the surface is a key factor affecting the CO_2ER[119-123]. The CO_2 electrochemical reduction consumes protons that can contribute to the accumulation of OH^- ions. The accumulated OH^- ions have been ascribed to inhibit the CO_2ER due to its reaction with the reactant CO_2, decreasing local CO_2 concentration near the active site.[124] Although the local pH near the surface of the electrode can be easily higher than the circumstance, measuring the pH changes around

the Nesrnest diffusion layer (thickness of 10^{-3} to 10^{-5}m) of the catalyst is a challenge. We deployed the rotating-ringing disc electrode (RRDE) technique to investigate the variation of local pH on two different catalysts. The principle of the RRDE assembly was described in **Figure 3.6** d. The catalyst was dropped on the glass carbon disk, and a constant potential was applied on the disk to convert CO_2 into CO. Under the centrifugal force conditions, cathodic product CO was transported to the anodic Pt ring and redox to CO_2 on the Pt ring. The CO oxidation is a pH-sensitive reaction. Thus, the variation of local pH of CO_2ER on the disk could be reflected by the CO oxidation reaction on the ring Pt electrode. It should be noted that the Pt easily oxidises H_2. To avoid the oxidation of H_2 at the Pt ring, the FE of CO must be near to 100%. Additionally, under the rotating condition, the force diffusion would boost the proton and CO_2 mass transfer, thus enhancing the overall CO_2 reduction performance. The CO_2ER process consumes protons. The excessive proton would not necessarily be converted into H_2. Therefore, the FE of CO changes little.[125]

To fabricate the RRDE assembly, 4 mg catalyst and 15 μL Nafion solution were introduced into 493.5μL ethanol and sonicated for at least 30 min. the 15μL well-dispersed ink was dropped onto glassy carbon disc (0.1256 cm^2) and dried in air. The experiment was performed in CO_2-saturated 0.5M $KHCO_3$ aqueous solutions. Under rotating conditions (2500 rpm), a constant potential (-0.4V to -0.6V) was applied on the catalyst disc to reduce CO_2, while a 0 to 1.567 V potential was applied on the Pt ring to oxide CO that was convectively transported from disc to the ring. The CVs on the Pt ring of p-Fe-N_x-C were shown in **Figure 3.6** e. The obvious oxidation peak for CO and

peak shift were observed. The potential of oxidation peak (E_p) on the Pt ring was determined by the concentration of formed CO and concurrent change in the local pH simultaneously. The E_p shifted positively with the increasing CO concentration, while E_p shifted negatively with the increase of local pH.[125] The relationships between E_p and the disc current density were illustrated in **Figure 3.6** f. The j_{CO2RR} of both catalysts were almost similar at -0.4V to -0.6V, which indicated the influence of CO concentration on the E_p shift for both catalysts were nearly the same. With the increase of current density on disk, the E_p of p-Fe-N_x-C shifted from 0.32V to 0.36 V, while that of s-Fe-N_x-C negatively shifted from 0.3V to 0.26V. This result indicated that the change of local pH for the p-Fe-N_x-C catalyst was not as remarkable as that for the s-Fe-N_x-C. The increase of local pH in the latter without abundant mesopores demonstrated the accumulation of OH^- ions at the catalyst/electrolyte interface, which might result in a relatively low CO_2 concentration and thus a low CO_2-to-CO conversion. These results were consistent with the EIS, and the CO_2 partial pressure related results discussed above. All of them revealed the importance of mesopores on Fe-single atoms catalysts for improved CO_2 reduction.

3.4 Conclusion

Pyrolysis of amorphous SiO_2 coated ZIF-8 is developed to synthesize N-doped carbon with a mesoporous structure. The absorption of the Fe-TPP molecules on N-doped carbon is an innovative method to obtain the Fe single-atom catalyst with mesopore, which is easy to control the numbers of Fe-N_x active sites. The p-Fe-N_x-C

and s-Fe-N_x-C exhibits excellent selectivity toward the CO_2-to-CO, with a Faradaic efficiency as high as 100% at -0.4V and -0.5V. Specifically, the current density of p-Fe-N_x-C is two times higher than the s-Fe-N_x-C. The results of RRDE experiments indicate the stable local pH on the p-Fe-N_x-C. The fast protons transfer contributes to the increased activity of the active sites in p-Fe-N_x-C. In addition, the electrochemical results of both catalysts in different CO_2 partial pressure (P_{CO2}) indicate that the mesopores can enhance the CO_2 transfer to achieve high catalytic activity. This work provides new evidence to explain the influence of the mesopore for CO_2ER and provide a rational idea to design cheap, efficient single-atom catalysts. In the future, the long-term stability of these samples will be investigated using a well-designed zero-gap MEA system.

Chapter 4 Conclusion and Outlook

4.1 Conclusion

This thesis has investigated several methods to synthesize Fe-N-C single-atom catalysts with porous structures for CO_2ER. Compared with the template method, the pyrolysis of amorphous SiO_2 coated ZIF-8 precursors is a simple and effective method to obtain the porous Fe-N-C catalyst (p-Fe-N_x-C). Enhanced electrocatalytic performance of the Fe-N-C catalyst was achieved by constructing the porous structure. A rotating ring-disk electrode was utilized to investigate the change of local pH near the catalysts' surface. The stable local pH was observed around the p-Fe-N_x-C catalyst during the CO_2ER, indicating the significantly facilitated proton transfer on the porous configuration. Furthermore, different CO_2 partial pressures were employed in the CO_2ER process, the results reveal the increased CO_2 transfer on the porous structure as well. Therefore, the porous structure can boost the CO_2 and proton transfer which further improve the CO_2ER performance of the Fe-N-C single-atom catalyst. This thesis offers a deeper understanding of the relationship between porosity and catalytic activity and provides an effective strategy to develop cheap and efficient electrocatalysts for CO_2ER.

4.2 Outlook

It is promising to develop efficient and cheap electrocatalysts to realize the conversion of CO_2 into a high-value product. Although Fe-N-C catalysts with porous structures achieve excellent CO_2ER performance, it is still challenging to achieve an industrial-scale performance. Future studies could be the focus on four directions.

First, it is still required to develop advanced single-atom electrocatalysts with a higher metal loading and/or enhanced intrinsic activity of metal sites. More active sites can be exposed in single-atom catalysts by constituting unique pores, shapes, and defects. Additionally, the development of advantageous coordination structures of M-N moieties is promising to enhance the intrinsic activity of metal sites

Second, the direct conversion of CO_2 into multi-carbon products suffers from CO_2 loss to carbonate in the alkaline electrolyte, contributing to the decrease of energy efficiency. Development of tandem system by coupling CO_2-to-CO conversion with CO-to-C2+ conversion product is a promising method to eliminate CO_2 loss to carbonate.[126] Compared with other catalysts, the single-atom catalysts exhibit superior advantages in the conversion of CO_2 into CO. Therefore, this cascade method using the single-atom catalysts for CO production is promising for industrial applications. The CO electroreduction to hydrocarbon process would become an attractive research area.

Third, it is highly desired to deepen the understanding of the mechanism of CO_2ER process, which will be beneficial to design electrocatalysts in the future. In the recent decade, *in situ* techniques have been significantly developed to investigate the CO_2ER mechanisms. For instance, in situ attenuated total reflection infrared spectroscopy

(ATR-IR) measurement has achieved extensive attention because it can directly offer structural information on the molecular-level of the electrode.[127], *In situ* Raman spectroscopy can be used to detect surface intermediates during CO_2 electrolysis, which can help researchers better understand the mechanism of CO_2ER.[128] Meanwhile, with the fast improvement of computer science and associated computational theories, the computational analysis of the CO_2ER process has also made tremendous progress. The density functional theory (DFT) has become a powerful tool to explain experimental results and predict potential catalysts.[16] The theoretical calculation combined with the results of advanced *in situ* techniques will facilitate understanding the relationships between the structure and performance of the catalyst, realizing the theory-guided design of electrocatalysts.

Finally, the catalysts of CO_2ER were estimated in the static H-cell where the performance is limited by the low solubility of CO_2 in aqueous solution and low CO_2 diffusion rate to the catalyst surface. To boost the catalytic performance of the CO_2ER, a gas diffusion electrode with a three-phase interface should be integrated into a flow cell. Currently, the flow cell has been applied in commercial-scale fuel cells and water electrolysis reactors. By addressing the challenges of mass transport in the H-Cell, a gaseous CO_2 input to the cathodic catalysts with considerably greater current density can be achieved in the flow cell.

Reference

1. Chu, S.; Majumdar, A., Opportunities and challenges for a sustainable energy future. *nature* **2012,** *488* (7411), 294-303.

2. Dresselhaus, M.; Thomas, I., Alternative energy technologies. *Nature* **2001,** *414* (6861), 332-337.

3. Graciani, J.; Mudiyanselage, K.; Xu, F.; Baber, A. E.; Evans, J.; Senanayake, S. D.; Stacchiola, D. J.; Liu, P.; Hrbek, J.; Sanz, J. F., Highly active copper-ceria and copper-ceria-titania catalysts for methanol synthesis from CO_2. *Science* **2014,** *345* (6196), 546-550.

4. Tans, E. D. a. P. NOAA/ESRL. https://gml.noaa.gov/ccgg/trends/.

5. Fernandez, J. R.; Garcia, S.; Sanz-Perez, E. S., CO_2 Capture and Utilization Editorial. ACS Publications: **2020**, 59 (15), 6767-6772

6. Bruhn, T.; Naims, H.; Olfe-Kräutlein, B., Separating the debate on CO_2 utilisation from carbon capture and storage. *Environmental Science & Policy* **2016,** *60*, 38-43.

7. Zhao, Y., Interface Engineering of Nanostructured Metal Catalysts for Improved CO_2 Electrochemical Reduction, Doctor of Philosophy thesis, Intelligent Polymer Research Institute, University of Wollongong, **2019**.

8. Aresta, M.; Dibenedetto, A.; Angelini, A., Catalysis for the valorization of exhaust carbon: from CO_2 to chemicals, materials, and fuels. Technological use of CO_2. *Chemical reviews* **2014,** *114* (3), 1709-1742.

9. Costentin, C.; Robert, M.; Savéant, J.-M., Catalysis of the electrochemical reduction of carbon dioxide. *Chemical Society Reviews* **2013,** *42* (6), 2423-2436.

10. Bushuyev, O. S.; De Luna, P.; Dinh, C. T.; Tao, L.; Saur, G.; van de Lagemaat, J.; Kelley, S. O.; Sargent, E. H., What should we make with CO_2 and how can we make it? *Joule* **2018,** *2* (5), 825-832.

11. Varela, A. S.; Ju, W.; Strasser, P., Molecular nitrogen–carbon catalysts, solid metal organic framework catalysts, and solid metal/nitrogen-doped carbon (MNC) catalysts for the electrochemical CO_2 reduction. *Advanced Energy Materials* **2018,** *8* (30), 1703614.

12. Agarwal, A. S.; Zhai, Y.; Hill, D.; Sridhar, N., The electrochemical reduction of carbon dioxide to formate/formic acid: engineering and economic feasibility. *ChemSusChem* **2011,** *4* (9), 1301-1310.

13. Qiao, J.; Liu, Y.; Hong, F.; Zhang, J., A review of catalysts for the electroreduction of carbon dioxide to produce low-carbon fuels. *Chemical Society Reviews* **2014,** *43* (2), 631-675.

14. Appel, A. M.; Bercaw, J. E.; Bocarsly, A. B.; Dobbek, H.; DuBois, D. L.; Dupuis, M.; Ferry, J. G.; Fujita, E.; Hille, R.; Kenis, P. J., Frontiers, opportunities, and challenges in biochemical and chemical catalysis of CO_2 fixation. *Chemical reviews* **2013,** *113* (8), 6621-6658.

15. Jia, C.; Dastafkan, K.; Ren, W.; Yang, W.; Zhao, C., Carbon-based catalysts for electrochemical CO_2 reduction. *Sustainable Energy & Fuels* **2019,** *3* (11), 2890-2906.

16. Zhu, D. D.; Liu, J. L.; Qiao, S. Z., Recent advances in inorganic heterogeneous electrocatalysts for reduction of carbon dioxide. *Advanced materials* **2016,** *28* (18), 3423-3452.

17. Wang, Z.-L.; Li, C.; Yamauchi, Y., Nanostructured nonprecious metal catalysts for electrochemical reduction of carbon dioxide. *Nano Today* **2016,** *11* (3), 373-391.

18. Manthiram, K.; Beberwyck, B. J.; Alivisatos, A. P., Enhanced electrochemical methanation of carbon dioxide with a dispersible nanoscale copper catalyst. *Journal of the American Chemical Society* **2014,** *136* (38), 13319-13325.

19. Schlögl, R., Heterogeneous catalysis. *Angewandte Chemie International Edition* **2015,** *54* (11), 3465-3520.

20. Benson, E. E.; Kubiak, C. P.; Sathrum, A. J.; Smieja, J. M., Electrocatalytic and homogeneous approaches to conversion of CO_2 to liquid fuels. *Chemical Society Reviews* **2009,** *38* (1), 89-99.

21. Dinh, C.-T.; Burdyny, T.; Kibria, M. G.; Seifitokaldani, A.; Gabardo, C. M.; De Arquer, F. P. G.; Kiani, A.; Edwards, J. P.; De Luna, P.; Bushuyev, O. S., CO_2 electroreduction to ethylene via hydroxide-mediated copper catalysis at an abrupt interface. *Science* **2018,** *360* (6390), 783-787.

22. Li, C. W.; Kanan, M. W., CO_2 reduction at low overpotential on Cu electrodes resulting from the reduction of thick Cu_2O films. *Journal of the American Chemical Society* **2012,** *134* (17), 7231-7234.

23. Chen, Y.; Li, C. W.; Kanan, M. W., Aqueous CO_2 reduction at very low overpotential on oxide-derived Au nanoparticles. *Journal of the American Chemical*

Society **2012,** *134* (49), 19969-19972.

24. Durst, J.; Rudnev, A.; Dutta, A.; Fu, Y.; Herranz, J.; Kaliginedi, V.; Kuzume, A.; Permyakova, A. A.; Paratcha, Y.; Broekmann, P., Electrochemical CO_2 reduction–a critical view on fundamentals, materials and applications. *CHIMIA International Journal for Chemistry* **2015,** *69* (12), 769-776.

25. Yang, Y.; Li, F., Reactor design for electrochemical CO_2 conversion toward large-scale applications. *Current Opinion in Green and Sustainable Chemistry* **2021,** *27*, 100419.

26. Akhade, S. A.; Luo, W.; Nie, X.; Bernstein, N. J.; Asthagiri, A.; Janik, M. J., Poisoning effect of adsorbed CO during CO_2 electroreduction on late transition metals. *Physical Chemistry Chemical Physics* **2014,** *16* (38), 20429-20435.

27. Chen, C. S.; Handoko, A. D.; Wan, J. H.; Ma, L.; Ren, D.; Yeo, B. S., Stable and selective electrochemical reduction of carbon dioxide to ethylene on copper mesocrystals. *Catalysis Science & Technology* **2015,** *5* (1), 161-168.

28. Gattrell, M.; Gupta, N.; Co, A., A review of the aqueous electrochemical reduction of CO_2 to hydrocarbons at copper. *Journal of electroanalytical Chemistry* **2006,** *594* (1), 1-19.

29. Hori, Y.; Takahashi, I.; Koga, O.; Hoshi, N., Selective formation of C2 compounds from electrochemical reduction of CO_2 at a series of copper single crystal electrodes. *The Journal of Physical Chemistry B* **2002,** *106* (1), 15-17.

30. Hori, Y. i., Electrochemical CO_2 reduction on metal electrodes. In *Modern aspects of electrochemistry*, Springer: **2008**; pp 89-189.

31. Hori, Y.; Kikuchi, K.; Suzuki, S., Production of CO and CH_4 in electrochemical reduction of CO_2 at metal electrodes in aqueous hydrogencarbonate solution. *Chemistry Letters* **1985,** *14* (11), 1695-1698.

32. Hori, Y.; Wakebe, H.; Tsukamoto, T.; Koga, O., Electrocatalytic process of CO selectivity in electrochemical reduction of CO_2 at metal electrodes in aqueous media. *Electrochimica Acta* **1994,** *39* (11-12), 1833-1839.

33. Kuhl, K. P.; Hatsukade, T.; Cave, E. R.; Abram, D. N.; Kibsgaard, J.; Jaramillo, T. F., Electrocatalytic conversion of carbon dioxide to methane and methanol on transition metal surfaces. *Journal of the American Chemical Society* **2014,** *136* (40), 14107-14113.

34. Lu, Q.; Rosen, J.; Jiao, F., Nanostructured metallic electrocatalysts for carbon dioxide reduction. *ChemCatChem* **2015,** *7* (1), 38-47.

35. He, J.; Johnson, N. J.; Huang, A.; Berlinguette, C. P., Electrocatalytic alloys for CO_2 reduction. *ChemSusChem* **2018,** *11* (1), 48-57.

36. Li, F.; MacFarlane, D. R.; Zhang, J., Recent advances in the nanoengineering of electrocatalysts for CO_2 reduction. *Nanoscale* **2018,** *10* (14), 6235-6260.

37. Jovanov, Z. P.; Hansen, H. A.; Varela, A. S.; Malacrida, P.; Peterson, A. A.; Nørskov, J. K.; Stephens, I. E.; Chorkendorff, I., Opportunities and challenges in the electrocatalysis of CO_2 and CO reduction using bifunctional surfaces: A theoretical and experimental study of Au–Cd alloys. *Journal of Catalysis* **2016,** *343*, 215-231.

38. Arrigo, R.; Schuster, M. E.; Wrabetz, S.; Girgsdies, F.; Tessonnier, J. P.; Centi, G.; Perathoner, S.; Su, D. S.; Schlögl, R., New insights from

microcalorimetry on the FeO_x/CNT-based electrocatalysts active in the conversion of CO_2 to fuels. *ChemSusChem* **2012,** *5* (3), 577-586.

39. Grace, A. N.; Choi, S. Y.; Vinoba, M.; Bhagiyalakshmi, M.; Chu, D. H.; Yoon, Y.; Nam, S. C.; Jeong, S. K., Electrochemical reduction of carbon dioxide at low overpotential on a polyaniline/Cu_2O nanocomposite based electrode. *Applied energy* **2014,** *120*, 85-94.

40. Kumari, N.; Sinha, N.; Haider, M. A.; Basu, S., CO_2 reduction to methanol on CeO_2 (110) surface: a density functional theory study. *Electrochimica Acta* **2015,** *177*, 21-29.

41. Ullah, N.; Ali, I.; Jansen, M.; Omanovic, S., Electrochemical reduction of CO_2 in an aqueous electrolyte employing an iridium/ruthenium-oxide electrode. *The Canadian Journal of Chemical Engineering* **2015,** *93* (1), 55-62.

42. Ma, S.; Lan, Y.; Perez, G. M.; Moniri, S.; Kenis, P. J., Silver supported on titania as an active catalyst for electrochemical carbon dioxide reduction. *ChemSusChem* **2014,** *7* (3), 866-874.

43. Ramesha, G. K.; Brennecke, J. F.; Kamat, P. V., Origin of catalytic effect in the reduction of CO_2 at nanostructured TiO2 films. *ACS Catalysis* **2014,** *4* (9), 3249-3254.

44. Chu, D.; Qin, G.; Yuan, X.; Xu, M.; Zheng, P.; Lu, J., Fixation of CO_2 by electrocatalytic reduction and electropolymerization in ionic liquid–H_2O solution. *ChemSusChem: Chemistry & Sustainability Energy & Materials* **2008,** *1* (3), 205-209.

45. Xu, J.; Li, X.; Liu, W.; Sun, Y.; Ju, Z.; Yao, T.; Wang, C.; Ju, H.; Zhu, J.; Wei, S., Carbon dioxide electroreduction into syngas boosted by a partially

delocalized charge in molybdenum sulfide selenide alloy monolayers. *Angewandte Chemie International Edition* **2017,** *56* (31), 9121-9125.

46. Asadi, M.; Kim, K.; Liu, C.; Addepalli, A. V.; Abbasi, P.; Yasaei, P.; Phillips, P.; Behranginia, A.; Cerrato, J. M.; Haasch, R., Nanostructured transition metal dichalcogenide electrocatalysts for CO_2 reduction in ionic liquid. *Science* **2016,** *353* (6298), 467-470.

47. Asadi, M.; Kumar, B.; Behranginia, A.; Rosen, B. A.; Baskin, A.; Repnin, N.; Pisasale, D.; Phillips, P.; Zhu, W.; Haasch, R., Robust carbon dioxide reduction on molybdenum disulphide edges. *Nature communications* **2014,** *5* (1), 1-8.

48. Abbasi, P.; Asadi, M.; Liu, C.; Sharifi-Asl, S.; Sayahpour, B.; Behranginia, A.; Zapol, P.; Shahbazian-Yassar, R.; Curtiss, L. A.; Salehi-Khojin, A., Tailoring the edge structure of molybdenum disulfide toward electrocatalytic reduction of carbon dioxide. *ACS nano* **2017,** *11* (1), 453-460.

49. Yamaguchi, A.; Yamamoto, M.; Takai, K.; Ishii, T.; Hashimoto, K.; Nakamura, R., Electrochemical CO_2 reduction by Ni-containing iron sulfides: How is CO_2 electrochemically reduced at bisulfide-bearing deep-sea hydrothermal precipitates? *Electrochimica Acta* **2014,** *141*, 311-318.

50. Lee, J.; Kim, J.; Hyeon, T., Recent progress in the synthesis of porous carbon materials. *Advanced materials* **2006,** *18* (16), 2073-2094.

51. Georgakilas, V.; Perman, J. A.; Tucek, J.; Zboril, R., Broad family of carbon nanoallotropes: classification, chemistry, and applications of fullerenes, carbon dots, nanotubes, graphene, nanodiamonds, and combined superstructures. *Chemical reviews*

2015, *115* (11), 4744-4822.

52. Wang, D. W.; Li, F.; Liu, M.; Lu, G. Q.; Cheng, H. M., 3D aperiodic hierarchical porous graphitic carbon material for high-rate electrochemical capacitive energy storage. *Angewandte Chemie International Edition* **2008,** *47* (2), 373-376.

53. Kumar, B.; Asadi, M.; Pisasale, D.; Sinha-Ray, S.; Rosen, B. A.; Haasch, R.; Abiade, J.; Yarin, A. L.; Salehi-Khojin, A., Renewable and metal-free carbon nanofibre catalysts for carbon dioxide reduction. *Nature communications* **2013,** *4* (1), 1-8.

54. Sreekanth, N.; Nazrulla, M. A.; Vineesh, T. V.; Sailaja, K.; Phani, K. L., Metal-free boron-doped graphene for selective electroreduction of carbon dioxide to formic acid/formate. *Chemical Communications* **2015,** *51* (89), 16061-16064.

55. Xu, J.; Kan, Y.; Huang, R.; Zhang, B.; Wang, B.; Wu, K.-H.; Lin, Y.; Sun, X.; Li, Q.; Centi, G., Revealing the origin of activity in nitrogen-doped nanocarbons towards electrocatalytic reduction of carbon dioxide. *ChemSusChem* **2016,** *9* (10), 1085-1089.

56. Li, F.; Xue, M.; Knowles, G. P.; Chen, L.; MacFarlane, D. R.; Zhang, J., Porous nitrogen–doped carbon derived from biomass for electrocatalytic reduction of CO_2 to CO. *Electrochimica Acta* **2017,** *245*, 561-568.

57. Sun, X.; Kang, X.; Zhu, Q.; Ma, J.; Yang, G.; Liu, Z.; Han, B., Very highly efficient reduction of CO_2 to CH_4 using metal-free N-doped carbon electrodes. *Chemical science* **2016,** *7* (4), 2883-2887.

58. Wang, H.; Jia, J.; Song, P.; Wang, Q.; Li, D.; Min, S.; Qian, C.; Wang,

L.; Li, Y. F.; Ma, C., Efficient electrocatalytic reduction of CO_2 by Nitrogen-doped nanoporous carbon/carbon nanotube membranes: a step towards the electrochemical CO_2 refinery. *Angewandte Chemie* **2017,** *129* (27), 7955-7960.

59. Wu, J.; Yadav, R. M.; Liu, M.; Sharma, P. P.; Tiwary, C. S.; Ma, L.; Zou, X.; Zhou, X.-D.; Yakobson, B. I.; Lou, J., Achieving highly efficient, selective, and stable CO_2 reduction on nitrogen-doped carbon nanotubes. *ACS nano* **2015,** *9* (5), 5364-5371.

60. Wu, J.; Liu, M.; Sharma, P. P.; Yadav, R. M.; Ma, L.; Yang, Y.; Zou, X.; Zhou, X.-D.; Vajtai, R.; Yakobson, B. I., Incorporation of nitrogen defects for efficient reduction of CO_2 via two-electron pathway on three-dimensional graphene foam. *Nano letters* **2016,** *16* (1), 466-470.

61. Wu, J.; Ma, S.; Sun, J.; Gold, J. I.; Tiwary, C.; Kim, B.; Zhu, L.; Chopra, N.; Odeh, I. N.; Vajtai, R., A metal-free electrocatalyst for carbon dioxide reduction to multi-carbon hydrocarbons and oxygenates. *Nature communications* **2016,** *7* (1), 1-6.

62. Liu, Y.; Chen, S.; Quan, X.; Yu, H., Efficient electrochemical reduction of carbon dioxide to acetate on nitrogen-doped nanodiamond. *Journal of the American Chemical Society* **2015,** *137* (36), 11631-11636.

63. Wang, H.; Chen, Y.; Hou, X.; Ma, C.; Tan, T., Nitrogen-doped graphenes as efficient electrocatalysts for the selective reduction of carbon dioxide to formate in aqueous solution. *Green Chemistry* **2016,** *18* (11), 3250-3256.

64. Nakata, K.; Ozaki, T.; Terashima, C.; Fujishima, A.; Einaga, Y., High-yield

electrochemical production of formaldehyde from CO_2 and seawater. *Angewandte Chemie International Edition* **2014,** *53* (3), 871-874.

65. Liu, Y.; Zhang, Y.; Cheng, K.; Quan, X.; Fan, X.; Su, Y.; Chen, S.; Zhao, H.; Zhang, Y.; Yu, H., Selective electrochemical reduction of carbon dioxide to ethanol on a boron-and nitrogen-Co-doped nanodiamond. *Angewandte Chemie* **2017,** *129* (49), 15813-15817.

66. Xie, J.; Zhao, X.; Wu, M.; Li, Q.; Wang, Y.; Yao, J., Metal-Free Fluorine-Doped Carbon Electrocatalyst for CO_2 Reduction Outcompeting Hydrogen Evolution. *Angewandte Chemie* **2018,** *130* (31), 9788-9792.

67. Peng, Y.; Lu, B.; Chen, S., Carbon-supported single atom catalysts for electrochemical energy conversion and storage. *Advanced Materials* **2018,** *30* (48), 1801995.

68. Chen, Y.; Ji, S.; Chen, C.; Peng, Q.; Wang, D.; Li, Y., Single-atom catalysts: synthetic strategies and electrochemical applications. *Joule* **2018,** *2* (7), 1242-1264.

69. Zhang, H.; Liu, G.; Shi, L.; Ye, J., Single-atom catalysts: emerging multifunctional materials in heterogeneous catalysis. *Advanced Energy Materials* **2018,** *8* (1), 1701343.

70. Li, H.; Zhang, H.-x.; Yan, X.-l.; Xu, B.-s.; Guo, J.-j., Carbon-supported metal single atom catalysts. *New Carbon Materials* **2018,** *33* (1), 1-11.

71. Su, J.; Ge, R.; Dong, Y.; Hao, F.; Chen, L., Recent progress in single-atom electrocatalysts: concept, synthesis, and applications in clean energy conversion. *Journal of Materials Chemistry A* **2018,** *6* (29), 14025-14042.

72. Varela, A. S.; Ranjbar Sahraie, N.; Steinberg, J.; Ju, W.; Oh, H. S.; Strasser, P., Metal-doped nitrogenated carbon as an efficient catalyst for direct CO_2 electroreduction to CO and hydrocarbons. *Angewandte Chemie International Edition* **2015,** *54* (37), 10758-10762.

73. Ju, W.; Bagger, A.; Hao, G.-P.; Varela, A. S.; Sinev, I.; Bon, V.; Cuenya, B. R.; Kaskel, S.; Rossmeisl, J.; Strasser, P., Understanding activity and selectivity of metal-nitrogen-doped carbon catalysts for electrochemical reduction of CO_2. *Nature communications* **2017,** *8* (1), 1-9.

74. Zhao, C.; Dai, X.; Yao, T.; Chen, W.; Wang, X.; Wang, J.; Yang, J.; Wei, S.; Wu, Y.; Li, Y., Ionic exchange of metal–organic frameworks to access single nickel sites for efficient electroreduction of CO_2. *Journal of the American Chemical Society* **2017,** *139* (24), 8078-8081.

75. Huan, T. N.; Ranjbar, N.; Rousse, G.; Sougrati, M.; Zitolo, A.; Mougel, V.; Jaouen, F.; Fontecave, M., Electrochemical reduction of CO_2 catalyzed by Fe-NC materials: A structure–selectivity study. *ACS catalysis* **2017,** *7* (3), 1520-1525.

76. Zhang, C.; Yang, S.; Wu, J.; Liu, M.; Yazdi, S.; Ren, M.; Sha, J.; Zhong, J.; Nie, K.; Jalilov, A. S., Electrochemical CO_2 reduction with atomic iron-dispersed on nitrogen-doped graphene. *Advanced Energy Materials* **2018,** *8* (19), 1703487.

77. Gu, J.; Hsu, C.-S.; Bai, L.; Chen, H. M.; Hu, X., Atomically dispersed Fe^{3+} sites catalyze efficient CO_2 electroreduction to CO. *Science* **2019,** *364* (6445), 1091-1094.

78. Jiao, Y.; Zheng, Y.; Jaroniec, M.; Qiao, S. Z., Design of electrocatalysts for oxygen-and hydrogen-involving energy conversion reactions. *Chemical Society Reviews* **2015,** *44* (8), 2060-2086.

79. Hu, C.; Bai, S.; Gao, L.; Liang, S.; Yang, J.; Cheng, S.-D.; Mi, S.-B.; Qiu, J., Porosity-Induced High Selectivity for CO_2 Electroreduction to CO on Fe-Doped ZIF-Derived Carbon Catalysts. *ACS Catalysis* **2019,** *9* (12), 11579-11588.

80. Cheng, Q.; Mao, K.; Ma, L.; Yang, L.; Zou, L.; Zou, Z.; Hu, Z.; Yang, H., Encapsulation of iron nitride by Fe–N–C shell enabling highly efficient electroreduction of CO_2 to CO. *ACS Energy Letters* **2018,** *3* (5), 1205-1211.

81. Li, E.; Yang, F.; Wu, Z.; Wang, Y.; Ruan, M.; Song, P.; Xing, W.; Xu, W., A bifunctional highly efficient FeNx/C electrocatalyst. *Small* **2018,** *14* (8), 1702827.

82. Pan, F.; Zhao, H.; Deng, W.; Feng, X.; Li, Y., A novel N, Fe-Decorated carbon nanotube/carbon nanosheet architecture for efficient CO_2 reduction. *Electrochimica Acta* **2018,** *273*, 154-161.

83. Li, X.; Bi, W.; Chen, M.; Sun, Y.; Ju, H.; Yan, W.; Zhu, J.; Wu, X.; Chu, W.; Wu, C., Exclusive Ni–N_4 sites realize near-unity CO selectivity for electrochemical CO_2 reduction. *Journal of the American Chemical Society* **2017,** *139* (42), 14889-14892.

84. Jiang, K.; Siahrostami, S.; Zheng, T.; Hu, Y.; Hwang, S.; Stavitski, E.; Peng, Y.; Dynes, J.; Gangisetty, M.; Su, D., Isolated Ni single atoms in graphene nanosheets for high-performance CO_2 reduction. *Energy & Environmental Science* **2018,** *11* (4), 893-903.

85. Yang, H. B.; Hung, S.-F.; Liu, S.; Yuan, K.; Miao, S.; Zhang, L.; Huang, X.; Wang, H.-Y.; Cai, W.; Chen, R., Atomically dispersed Ni (I) as the active site for electrochemical CO_2 reduction. *Nature energy* **2018,** *3* (2), 140-147.

86. Su, P.; Iwase, K.; Nakanishi, S.; Hashimoto, K.; Kamiya, K., Nickel-nitrogen-modified graphene: an efficient electrocatalyst for the reduction of carbon dioxide to carbon monoxide. *Small* **2016,** *12* (44), 6083-6089.

87. Yan, C.; Li, H.; Ye, Y.; Wu, H.; Cai, F.; Si, R.; Xiao, J.; Miao, S.; Xie, S.; Yang, F., Coordinatively unsaturated nickel–nitrogen sites towards selective and high-rate CO_2 electroreduction. *Energy & Environmental Science* **2018,** *11* (5), 1204-1210.

88. Bi, W.; Li, X.; You, R.; Chen, M.; Yuan, R.; Huang, W.; Wu, X.; Chu, W.; Wu, C.; Xie, Y., Surface immobilization of transition metal ions on nitrogen-doped graphene realizing high-efficient and selective CO_2 reduction. *Advanced Materials* **2018,** *30* (18), 1706617.

89. Wang, X.; Chen, Z.; Zhao, X.; Yao, T.; Chen, W.; You, R.; Zhao, C.; Wu, G.; Wang, J.; Huang, W., Regulation of coordination number over single Co sites: triggering the efficient electroreduction of CO_2. *Angewandte Chemie* **2018,** *130* (7), 1962-1966.

90. Pan, Y.; Lin, R.; Chen, Y.; Liu, S.; Zhu, W.; Cao, X.; Chen, W.; Wu, K.; Cheong, W.-C.; Wang, Y., Design of single-atom Co–N_5 catalytic site: a robust electrocatalyst for CO_2 reduction with nearly 100% CO selectivity and remarkable stability. *Journal of the American chemical society* **2018,** *140* (12), 4218-4221.

91. Su, P.; Iwase, K.; Harada, T.; Kamiya, K.; Nakanishi, S., Covalent triazine framework modified with coordinatively-unsaturated Co or Ni atoms for CO_2 electrochemical reduction. *Chemical science* **2018,** *9* (16), 3941-3947.

92. Song, H.; Im, M.; Song, J. T.; Lim, J.-A.; Kim, B.-S.; Kwon, Y.; Ryu, S.; Oh, J., Effect of mass transfer and kinetics in ordered Cu-mesostructures for electrochemical CO_2 reduction. *Applied Catalysis B: Environmental* **2018,** *232*, 391-396.

93. Hursán, D.; Samu, A. A.; Janovák, L.; Artyushkova, K.; Asset, T.; Atanassov, P.; Janáky, C., Morphological attributes govern carbon dioxide reduction on N-doped carbon electrodes. *Joule* **2019,** *3* (7), 1719-1733.

94. Hossain, M. N.; Liu, Z.; Wen, J.; Chen, A., Enhanced catalytic activity of nanoporous Au for the efficient electrochemical reduction of carbon dioxide. *Applied Catalysis B: Environmental* **2018,** *236*, 483-489.

95. Daiyan, R.; Lu, X.; Saputera, W. H.; Ng, Y. H.; Amal, R., Highly selective reduction of CO_2 to formate at low overpotentials achieved by a mesoporous tin oxide electrocatalyst. *ACS Sustainable Chemistry & Engineering* **2018,** *6* (2), 1670-1679.

96. Naseem, F.; Lu, P.; Zeng, J.; Lu, Z.; Ng, Y. H.; Zhao, H.; Du, Y.; Yin, Z., Solid nanoporosity governs catalytic CO_2 and N_2 reduction. *ACS nano* **2020,** *14* (7), 7734-7759.

97. Raval, N.; Maheshwari, R.; Kalyane, D.; Youngren-Ortiz, S. R.; Chougule, M. B.; Tekade, R. K., Importance of physicochemical characterization of nanoparticles in pharmaceutical product development. In *Basic Fundamentals of Drug Delivery*,

Elsevier: **2019**; pp 369-400.

98. Misof, B.; Roschger, P.; Fratzl, P., Imaging mineralized tissues in vertebrates. In *Comprehensive Biomaterials II*, Elsevier: **2017**; pp 549-578.

99. Asoro, M.; Kovar, D.; Shao-Horn, Y.; Allard, L.; Ferreira, P., Coalescence and sintering of Pt nanoparticles: in situ observation by aberration-corrected HAADF STEM. *Nanotechnology* **2009,** *21* (2), 025701.

100. Asefa, T.; Dubovoy, V., Ordered Mesoporous/Nanoporous Inorganic Materials via Self-Assembly. In *Nanotechnology*, Elsevier Inc.: **2017**; pp 158-192.

101. Ren, W.; Tan, X.; Yang, W.; Jia, C.; Xu, S.; Wang, K.; Smith, S. C.; Zhao, C., Isolated diatomic Ni-Fe metal–nitrogen sites for synergistic electroreduction of CO_2. *Angewandte Chemie International Edition* **2019,** *58* (21), 6972-6976.

102. Lu, P.; Yang, Y.; Yao, J.; Wang, M.; Dipazir, S.; Yuan, M.; Zhang, J.; Wang, X.; Xie, Z.; Zhang, G., Facile synthesis of single-nickel-atomic dispersed N-doped carbon framework for efficient electrochemical CO_2 reduction. *Applied Catalysis B: Environmental* **2019,** *241*, 113-119.

103. Fei, H.; Dong, J.; Chen, D.; Hu, T.; Duan, X.; Shakir, I.; Huang, Y.; Duan, X., Single atom electrocatalysts supported on graphene or graphene-like carbons. *Chemical Society Reviews* **2019,** *48* (20), 5207-5241.

104. Costentin, C.; Robert, M.; Savéant, J.-M.; Tatin, A., Efficient and selective molecular catalyst for the CO_2-to-CO electrochemical conversion in water. *Proceedings of the National Academy of Sciences* **2015,** *112* (22), 6882-6886.

105. Costentin, C.; Passard, G.; Robert, M.; Savéant, J.-M., Ultraefficient

homogeneous catalyst for the CO_2-to-CO electrochemical conversion. *Proceedings of the National Academy of Sciences* **2014,** *111* (42), 14990-14994.

106. Hu, X.-M.; Hval, H. H.; Bjerglund, E. T.; Dalgaard, K. J.; Madsen, M. R.; Pohl, M.-M.; Welter, E.; Lamagni, P.; Buhl, K. B.; Bremholm, M., Selective CO_2 reduction to CO in water using earth-abundant metal and nitrogen-doped carbon electrocatalysts. *ACS catalysis* **2018,** *8* (7), 6255-6264.

107. Kramm, U. I.; Herrmann-Geppert, I.; Behrends, J.; Lips, K.; Fiechter, S.; Bogdanoff, P., On an easy way to prepare metal–nitrogen doped carbon with exclusive presence of MeN_4-type sites active for the ORR. *Journal of the American Chemical Society* **2016,** *138* (2), 635-640.

108. Pan, F.; Zhang, H.; Liu, K.; Cullen, D.; More, K.; Wang, M.; Feng, Z.; Wang, G.; Wu, G.; Li, Y., Unveiling active sites of CO_2 reduction on nitrogen-coordinated and atomically dispersed iron and cobalt catalysts. *Acs Catalysis* **2018,** *8* (4), 3116-3122.

109. Qu, Q.; Min, Y.; Zhang, L.; Xu, Q.; Yin, Y., Silica microspheres with fibrous shells: synthesis and application in HPLC. *Analytical chemistry* **2015,** *87* (19), 9631-9638.

110. Jezequel, D.; Guenot, J.; Jouini, N.; Fievet, F., Preparation and Morphological Characterization of Fine, Spherical, Monodisperse Particles of ZnO. *Materials Science Forum* **1994,** *152-153*, 339-342.

111. Seelig, E. W.; Tang, B.; Yamilov, A.; Cao, H.; Chang, R. P. H., Self-assembled 3D photonic crystals from ZnO colloidal spheres. *Materials Chemistry and*

Physics **2003,** *80* (1), 257-263.

112. Wang, X.; Liu, J.; Leong, S.; Lin, X.; Wei, J.; Kong, B.; Xu, Y.; Low, Z. X.; Yao, J.; Wang, H., Rapid Construction of ZnO@ZIF-8 Heterostructures with Size-Selective Photocatalysis Properties. *ACS Appl Mater Interfaces* **2016,** *8* (14), 9080-9087.

113. Li, Z.; Zeng, H. C., Armored MOFs: enforcing soft microporous MOF nanocrystals with hard mesoporous silica. *Journal of the American Chemical Society* **2014,** *136* (15), 5631-5639.

114. Wan, X.; Liu, X.; Li, Y.; Yu, R.; Zheng, L.; Yan, W.; Wang, H.; Xu, M.; Shui, J., Fe–N–C electrocatalyst with dense active sites and efficient mass transport for high-performance proton exchange membrane fuel cells. *Nature Catalysis* **2019,** *2* (3), 259-268.

115. Chen, Y.; Ji, S.; Wang, Y.; Dong, J.; Chen, W.; Li, Z.; Shen, R.; Zheng, L.; Zhuang, Z.; Wang, D., Isolated single iron atoms anchored on N-doped porous carbon as an efficient electrocatalyst for the oxygen reduction reaction. *Angewandte Chemie* **2017,** *129* (24), 7041-7045.

116. Zhang, C.; Wang, Y. C.; An, B.; Huang, R.; Wang, C.; Zhou, Z.; Lin, W., Networking pyrolyzed zeolitic imidazolate frameworks by carbon nanotubes improves conductivity and enhances oxygen-reduction performance in polymer-electrolyte-membrane fuel cells. *Advanced Materials* **2017,** *29* (4), 1604556.

117. Han, L.; Song, S.; Liu, M.; Yao, S.; Liang, Z.; Cheng, H.; Ren, Z.; Liu, W.; Lin, R.; Qi, G., Stable and efficient single-atom Zn catalyst for CO_2 reduction

to CH_4. *Journal of the American Chemical Society* **2020,** *142* (29), 12563-12567.

118. Wuttig, A.; Yaguchi, M.; Motobayashi, K.; Osawa, M.; Surendranath, Y., Inhibited proton transfer enhances Au-catalyzed CO_2-to-fuels selectivity. *Proceedings of the National Academy of Sciences* **2016,** *113* (32), E4585-E4593.

119. Billy, J. T.; Co, A. C., Experimental parameters influencing hydrocarbon selectivity during the electrochemical conversion of CO_2. *ACS Catalysis* **2017,** *7* (12), 8467-8479.

120. Ayemoba, O.; Cuesta, A., Spectroscopic evidence of size-dependent buffering of interfacial pH by cation hydrolysis during CO_2 electroreduction. *ACS applied materials & interfaces* **2017,** *9* (33), 27377-27382.

121. Singh, M. R.; Kwon, Y.; Lum, Y.; Ager III, J. W.; Bell, A. T., Hydrolysis of electrolyte cations enhances the electrochemical reduction of CO_2 over Ag and Cu. *Journal of the American Chemical Society* **2016,** *138* (39), 13006-13012.

122. Kas, R.; Kortlever, R.; Yılmaz, H.; Koper, M. T.; Mul, G., Manipulating the hydrocarbon selectivity of copper nanoparticles in CO_2 electroreduction by process conditions. *ChemElectroChem* **2015,** *2* (3), 354-358.

123. Dunwell, M.; Yang, X.; Setzler, B. P.; Anibal, J.; Yan, Y.; Xu, B., Examination of near-electrode concentration gradients and kinetic impacts on the electrochemical reduction of CO2 using surface-enhanced infrared spectroscopy. *Acs Catalysis* **2018,** *8* (5), 3999-4008.

124. Singh, M. R.; Clark, E. L.; Bell, A. T., Effects of electrolyte, catalyst, and membrane composition and operating conditions on the performance of solar-driven

electrochemical reduction of carbon dioxide. *Physical Chemistry Chemical Physics* **2015,** *17* (29), 18924-18936.

125. Zhang, F.; Co, A. C., Direct evidence of local pH change and the role of alkali cation during CO_2 electroreduction in aqueous media. *Angewandte Chemie International Edition* **2020,** *59* (4), 1674-1681.

126. Ozden, A.; Wang, Y.; Li, F.; Luo, M.; Sisler, J.; Thevenon, A.; Rosas-Hernández, A.; Burdyny, T.; Lum, Y.; Yadegari, H., Cascade CO_2 electroreduction enables efficient carbonate-free production of ethylene. *Joule* **2021,** *5* (3), 706-719.

127. Wang, H.; Zhou, Y.-W.; Cai, W.-B., Recent applications of in situ ATR-IR spectroscopy in interfacial electrochemistry. *Current Opinion in Electrochemistry* **2017,** *1* (1), 73-79.

128. Ren, D.; Deng, Y.; Handoko, A. D.; Chen, C. S.; Malkhandi, S.; Yeo, B. S., Selective electrochemical reduction of carbon dioxide to ethylene and ethanol on copper (I) oxide catalysts. *Acs Catalysis* **2015,** *5* (5), 2814-2821.